Materials & Design 260 (2025) 115273

Contents lists available at ScienceDirect

Materials & Design

journal homepage: www.elsevier.com/locate/matdes

A 3D-printed composite scaffold with sequential release of graphene oxide/hydroxyapatite synergistically enhances angiogenesis-osteogenesis for bone defect repair

Chunchun Li [a,1], Cuiting Lyu [e,1], Yangfan Ding [b,1], Ziying Feng [f], Jinzan Zhu [a], Yichen Zhao [a], Mohamed EL-Newehy [g], Meera Moydeen Abdulhameed [g], Duyao Su [a], Pengfei Cai [b,d,*], Xiumei Mo [b,c,**], Liang Song [a,***]

[a] Department of Stomatology, Shanghai Fifth People's Hospital, Fudan University, Shanghai 200240, China
[b] State Key Laboratory of Advanced Fibers Materials, Shanghai Engineering Research Center of Nano-Biomaterials and Regenerative Medicine, College of Biological Science and Medical Engineering, Donghua University, 201620 Shanghai, China
[c] Institute of Biomaterials and Biomedicine, School of Food and Pharmacy, Shanghai Zhongqiao Vocational and Technical University, 3888 Caolang Rd., Shanghai 201514, China
[d] G.E.R.N. Research Center for Tissue Replacement, Regeneration & Neogenesis, Department of Orthopedics and Trauma Surgery, Faculty of Medicine, Medical Center-Albert-Ludwigs- University of Freiburg, 79085 Freiburg im Breisgau, Germany
[e] Central Laboratory, Shanghai Fifth People's Hospital, Fudan University, Shanghai 200240, China
[f] Department of Stomatology, Shantou Central Hospital, Shantou, Guangdong Province 515041, China
[g] Department of Chemistry, College of Science, King Saud University, P.O. Box 2455, Riyadh 11451, Saudi Arabia

ARTICLE INFO

Keywords:
Tissue engineering
3D printing
Graphene oxide
Angiogenesis
Bone regeneration

ABSTRACT

Angiogenic and osteogenic factors coordinate bone repair through time-dependent regulation of cellular responses, ensuring synchronized neovascularization and osteogenesis. Therefore, we designed a framework using polycaprolactone (PCL) and hydroxyapatite (HAp), which was then filled with a gelatin (GEL) matrix containing graphene oxide (GO) (PH/GO scaffold). The GEL matrix rapidly degrades in the early stage, releasing GO to enhance the migration of vascular endothelial cells and promote the expression of angiogenic factors to stimulate early angiogenesis. The continuous release of HAp from the PCL framework promotes osteoblast differentiation by enhancing expression of bone-specific proteins and matrix mineralization. *In vivo* studies confirmed that PH/GO-1 (1%GO) significantly elevates the expression of early angiogenic factors and accelerates new bone formation during defect healing. This scaffold synergistically enhances angiogenesis and osteogenesis via spatiotemporal release, demonstrating superior regenerative capacity. It enables sustained delivery of key bioactive molecules, offering a promising biomaterial strategy for critical-sized bone defect repair.

1. Introduction

Bone tissue is one of the most critical structural and functional tissues in the human body, with primary roles including mechanical support, organ protection, locomotion facilitation, and mineral metabolism regulation [1]. Bone defects are commonly caused by trauma, tumor resection, or chronic inflammation [2]. When defect dimensions exceed the body's innate regenerative capacity, the biomechanical and physiological functions of bone are severely compromised, leading to significant negative impacts on patients' quality of life. Current clinical strategies for bone defect repair include autologous bone grafting, allogeneic bone transplantation, and metallic prosthesis implantation

* Corresponding author at: State Key Laboratory of Advanced Fibers Materials, Shanghai Engineering Research Center of Nano-Biomaterials and Regenerative Medicine, College of Biological Science and Medical Engineering, Donghua University, 201620 Shanghai, China.
** Corresponding author at: Institute of Biomaterials and Biomedicine, School of Food and Pharmacy, Shanghai Zhongqiao Vocational and Technical University, 3888 Caolang Rd., Shanghai 201514, China.
*** Corresponding author at: Department of Stomatology, Shanghai Fifth People's Hospital, Fudan University, Shanghai 200240, China.
E-mail addresses: cpfzzz1@163.com (P. Cai), xmm@dhu.edu.cn (X. Mo), sky_songliang@hotmail.com (L. Song).
[1] These authors contributed equally to this study.

https://doi.org/10.1016/j.matdes.2025.115273
Received 28 September 2025; Received in revised form 11 November 2025; Accepted 4 December 2025
Available online 5 December 2025

[3]. However, limitations such as insufficient donors, immune rejection, and suboptimal biocompatibility restrict their clinical application [4].

Bone tissue engineering offers an innovative paradigm to overcome the shortcomings of traditional repair strategies, with advantages including abundant material sources and avoidance of secondary surgical trauma [5]. Cytokines, seed cells, and scaffolds constitute the three core elements of bone tissue engineering, in which scaffolds, as the 3D support structure for bone regeneration, play a crucial role [6]. To achieve optimal regenerative outcomes, researchers have refined scaffold performance through material selection, microarchitecture design, surface modification, and fabrication technologies [7]. Additionally, 3D printing technology enables precise customization of implants tailored to patient-specific defects. It can also simulate the microstructure of natural bone and effectively promote the attachment, proliferation and differentiation of cells in the defect area [8].

Polycaprolactone (PCL) has been widely applied in bone tissue engineering due to its superior mechanical properties, biocompatibility, and controllable biodegradability [9]. HAp, a calcium phosphate-based bioceramic that mirrors the chemical composition and crystallographic features of native bone tissue, has attracted considerable attention for its excellent biocompatibility and osteoconductivity [10]. Bone defect repair involves a complex multi-stage biological process comprising inflammatory, reparative, and remodeling phases, with the reparative phase playing a pivotal role [11]. During this stage, angiogenesis serves as the cornerstone of bone repair by delivering cells, bioactive factors, and nutrients to the defect area, initiating and sustaining bone regeneration [12]. Subsequent osteoblast proliferation, bone matrix deposition, and tissue remodeling ultimately achieve complete bone regeneration and functional recovery. GO, a derivative of graphene via oxidative modification, has garnered significant attention in bone tissue engineering due to its pro-angiogenic capability that enhances blood supply and nutrient delivery to bone defect regions, thereby improving bone regeneration efficiency [13].

Currently, the combination of pro-angiogenic and pro-osteogenic components has become a prevalent trend. For instance, Chen et al. homogeneously mixed nHA and vascular endothelial growth factor (VEGF) into GelMA hydrogel to achieve synchronous release, thereby promoting both osteogenesis and angiogenesis simultaneously [14]. However, such designs mix all bioactive components in a single matrix, resulting in synchronous release kinetics, which may not optimally match the strictly time-sequenced physiological cascade inherent in bone healing.Therefore, the structural design of this study leverages the rapid degradation property of GEL and the slow degradation property of PCL. By physically separating the 3D-printed PCL/HAp framework from the freeze-dried GEL/GO components, this design enables the differentiation of the release kinetics of these two key bioactive elements. The 3D-printed PCL-hydroxyapatite (PH) scaffold framework provides mechanical support and sustains the release of calcium ions to facilitate osteogenesis. More critically, through the encapsulation of GEL/GO components within the scaffold cavities, the rapid degradation kinetics of GEL during the early reparative phase is exploited to release GO, thereby enhancing angiogenesis to initiate and sustain bone regeneration. This design effectively meets the stage-specific biological requirements by regulating the release kinetics and temporal dynamics of bioactive substances. 3D printing technology enables precise anatomical customization to match the defect morphology, while freeze-drying technology generates porous structures that promote cell adhesion, proliferation, and differentiation [15]. By integrating 3D printing and freeze-drying technologies, the scaffold constructs an optimal microenvironment conducive to angiogenesis and osteogenesis, which has been demonstrated to significantly enhance regenerative potential through synergistic mechanisms.

In this study, comprehensive physicochemical characterization and in vitro experiments will evaluate the scaffold's mechanical properties, biocompatibility, angiogenic capacity, and osteogenic performance. Then practical efficacy will be validated *in vivo* to assess its feasibility and effectiveness in defect repair. Our systematic evaluation will provide both theoretical and experimental support for future potential clinical applications.

2. Materials and Methods

2.1. Materials

PCL (Mn = 45,000), GEL (Type A) were purchased from Sigma-Aldrich (US). GO was purchased from Macklin Co., Ltd. (Shanghai, China). HAp (<100 nm) was purchased from Aladdin Co., Ltd. (Shanghai, China). Rat retinal vascular endothelial cells (rRMECs) and rat bone marrow mesenchymal stem cells (rBMSCs) were obtained from Wuhan Procell Life Sciences Co., Ltd.

2.2. Preparation of scaffolds

2.2.1. Preparation of pH frameworks

HAp and PCL were dissolved in dichloromethane at a mass ratio of 1:10 and stirred continuously for 3 h at room temperature to ensure adequate mixing. After freeze-drying the mixture, the PCL/HAp composite material was prepared. Subsequently, the composite material was cut into appropriately sized small pieces for subsequent 3D printing. The key parameters of the 3D printing process were as follows: 22-gauge injection nozzle was used, the printing temperature was set at 70 °C, the platform temperature was maintained at 25 °C (room temperature), the extrusion pneumatic pressure was set at 0.4 MPa, the layer height was 400 μm, and the printing filament spacing was 500 μm. The printing path angle was configured with alternating angles of 45°/−45°. Additionally, to ensure the uniform dispersion of HAp and prevent nozzle clogging, the PCL/HAp mixture was thoroughly mechanically stirred before being loaded into the printer. Ultimately, the PCL/HAp composite 3D printed scaffold (referred to as PH frame) was finally prepared.

2.2.2. Preparation of GO filling material

The GEL and deionized water were mixed at a mass ratio of 1:10 and stirred under a 40 °C water bath until complete dissolution to prepare a homogeneous GEL solution. Subsequently, GO was added to 10 ml of the GEL solution at different mass proportions (0, 100, and 200 mg). The mixtures were ultrasonically dispersed for 30 min to ensure uniform distribution, ultimately yielding dispersed solutions containing varying mass fractions of GO (0 %, 1 %, and 2 %).

2.2.3. Preparation of PH/GO composite scaffold

The 0 %, 1 %, and 2 % GO dispersed solutions were slowly dripped into the PH scaffolds, respectively. After the solution fully wetted the scaffold, the scaffolds were placed in a −80 °C freezer for cryogenic solidification. The frozen scaffolds were freeze-dried and then cross-linked using 1-ethyl-3-(3-dimethylaminopropyl) carbodiimide hydrochloride (EDC) and N-hydroxysuccinimide (NHS). Subsequently, the scaffolds were thoroughly rinsed with deionized water three times to remove residual EDC/NHS cross-linking agents. Finally, the GO composite scaffolds (denoted as PH/GO-0, PH/GO-1, and PH/GO-2) were obtained.

2.3. Characterization of PH/GO composite scaffold

2.3.1. Morphology of the scaffolds

The general appearance of the PH/GO-0, PH/GO-1 and PH/GO-2 scaffolds was captured using a digital camera. The microstructure of the scaffolds was observed by scanning electron microscopy (SEM, Phenom, Netherlands) at an accelerating voltage of 5 kV to evaluate the microstructural of composite 3D printed scaffolds [16].

2.3.2. Mechanical properties

The mechanical properties of the filled and unfilled scaffolds were

tested using a universal testing machine (Instron 5567, Norwood, MA, USA) [17]. Uniaxial compression was performed at a constant crosshead speed of 2 mm/min until 50 % strain was reached. Compression strength and compression modulus were calculated from the compression curves. Three replicate tests were performed for each group. Herein, the definitions of two scaffold types are clarified as follows: Uncasted scaffold refers to the framework fabricated solely by 3D printing of the PCL/HAp composite material. Casted scaffold denotes the composite scaffold obtained by filling the pores of the uncasted scaffold with GEL matrix followed by freeze-drying treatment.

2.3.3. Thermogravimetric analysis (TGA) and derivative thermogravimetry (DTG)

TGA of the PH/GO-0, PH/GO-1, and PH/GO-2 scaffolds was conducted in nitrogen using a thermogravimetric analyzer PerkinElmer TGA8000 (PerkinElmer Enterprise Management Co. Ltd., Shanghai, China). The temperature range was set from 30 °C to 800 °C with a heating rate of 5 °C/min [18]. Thermogravimetric parameters were analyzed based on the TGA curves.

2.3.4. Water contact angle

The surface water contact angle of the PH/GO-0, PH/GO-1, and PH/GO-2 stents was measured using a contact angle analyzer (DSA30, KRÜSS, Germany) by depositing 5 μl of deionized water onto the scaffold surfaces [19]. Three replicates were performed for each group.

2.3.5. Porosity and water absorption

The porosity of PH/GO-0, PH/GO-1, and PH/GO-2 scaffolds was determined via the liquid displacement method using cylindrical cast scaffolds [20]. Briefly, the diameter (d), height (h), and dry weight (m_a) of the scaffolds were measured. The scaffolds were then immersed in anhydrous ethanol. After removal from ethanol, excess liquid on the scaffold surfaces was gently blotted with filter paper, and the wet weight (m_b) was recorded. The porosity was calculated using the following formula:

$$Porosity\ (\%) = \frac{m_b - m_a}{\rho_{ethanol} \times \left(\frac{d}{2}\right)^2 \times h \times \pi} \times 100\%$$

The water absorption of PH/GO-0, PH/GO-1, and PH/GO-2 scaffolds was determined as follow: the dry scaffold mass (m_0) was measured, and the scaffold was then immersed in deionized water; at different time points, excess surface moisture on the samples was gently blotted with filter paper, and the wet mass (m_1) was recorded [20]. The water absorption capacity was calculated using the following formula:

$$Water\ absorption\ capacity\ (\%) = \frac{m_1 - m_0}{m_0} \times 100\%$$

2.3.6. Hemolysis assay

To evaluate the blood compatibility of PH/GO-0, PH/GO-1, and PH/GO-2 scaffolds, 5 ml of fresh blood from Sprague Dawley (SD) rats was collected in anticoagulant tubes and diluted with sterile phosphate-buffered saline (PBS, pH 7.4) at a 1:1 vol ratio. Sterilized scaffolds from each group were placed in test tubes, and 5 ml of sterile PBS was added, followed by incubation at 37 °C for 30 min. Positive and negative control groups were prepared using 5 ml of pure water (without scaffolds) and 5 ml of sterile PBS (without scaffolds), respectively. Subsequently, 0.2 ml of the diluted blood was added to each test tube. After incubation at 37 °C for 60 min, the tubes were centrifuged at 3000 rpm for 5 min. The supernatant of each sample was observed, photographed, and its optical density (OD) value was measured at a wavelength of 545 nm using a spectrophotometer (with five replicates per group) [17]. The hemolysis rate (HR) was calculated using the following formula:

$$\boldsymbol{HR}\ (\%) = \frac{OD_{material} - OD_{negative}}{OD_{positive} - OD_{negative}} \times 100\%$$

2.3.7. Degradation test

To evaluate the degradation behavior of each group of PH/GO composite scaffold, the dried scaffolds were cut into identically sized pieces, and their initial mass (m_0) was recorded. After sterilization under ultraviolet light for 1 h, the samples were prepared for degradation testing. Samples were placed in centrifuge tubes containing 2 ml of sterile PBS and incubated in a constant-temperature shaking incubator at 37 °C and 100 rpm. Specimens from each group were retrieved after 7, 14, 28, 60, and 90 days of degradation, rinsed with deionized water, and freeze-dried [18]. The post-degradation mass (m_1) of each group was then measured. Triplicate tests were conducted for each group, and average values were calculated. The degradation rate was determined using the following formula:

$$Degradation\ rate\ (\%) = \frac{m_0 - m_1}{m_0} \times 100\%$$

2.3.8. Ion release test

Dried composite scaffolds were cut into pieces of equal mass, followed by sterilization under ultraviolet light for 1 h. Subsequently, all test samples were placed in centrifuge tubes containing 2 ml of sterile PBS. These tubes were incubated in a constant-temperature shaking incubator at 37 °C and 100 rpm. At 14, 28, 60, and 90 days, the incubation solutions were collected and replaced with an equal volume of fresh PBS. The collected solutions were analyzed using inductively coupled plasma atomic emission spectrometry (ICP-AES, Prodigy Plus, Leeman, USA) to quantitatively determine the calcium ion concentration released from the PH/GO composite scaffold. Triplicate tests were performed for each group.

2.4. In vitro cytocompatibility of PH/GO scaffold

2.4.1. In vitro cell culture

The rRMECs were cultured in high-glucose DMEM medium supplemented with 10 % fetal bovine serum (FBS) and 1 % penicillin–streptomycin. rBMSCs were cultured in α-MEM medium containing 10 % FBS. Both cell types were maintained in a humidified incubator at 37 °C with 5 % CO_2, and the culture medium was replaced every other day to sustain cell growth.

2.4.2. Cell proliferation assay

The rRMECs and rBMSCs were seeded into 96-well plates at a density of 2×10^3 cells per well. After 24 h of incubation, the culture medium was replaced with extracted medium from PH/GO-0, PH/GO-1, and PH/GO-2 scaffolds. On days 1, 3, and 5 of culture, the old medium was removed, and the cells were washed twice with PBS. Subsequently, 10 % (v/v) CCK-8 reagent-containing medium was added, followed by incubation in the dark at 37 °C for 1.5 h. The absorbance of each group was then measured at 450 nm using a microplate reader.

2.4.3. Live/dead fluorescence staining

The rRMECs and rBMSCs were seeded into 48-well plates at a density of 1×10^4 cells per well. After 24 h of culture, the medium was replaced with extracted medium from PH/GO-0, PH/GO-1, and PH/GO-2 scaffolds. On days 1, 3, and 5, cells were washed three times with PBS and stained using the Calcein-AM/PI dual staining kit according to the manufacturer's instructions to assess cell viability. The fluorescent signals of cells were observed under a fluorescence microscope, with green fluorescence indicating live cells and red fluorescence representing dead cells [21].

2.4.4. Colony formation assay

The rRMECs and rBMSCs were seeded into 6-well plates at a density of 3×10^2 cells per well. After 24 h, the medium was replaced with scaffold extracts. Following 7 days of culture, cells were washed three times with PBS, fixed with anhydrous methanol for 15 min, and stained with 1 ml of 0.1 % (w/v) crystal violet solution per well. Stained colonies were subsequently imaged and analyzed.

2.5. In vitro angiogenic effects of PH/GO scaffold

2.5.1. Scratch wound assay

The rRMECs were seeded into 6-well plates at 3×10^5 cells per well. After 24 h, a linear wound was created in the confluent cell monolayer using a 200 μl pipette tip. Cells were washed three times with PBS, and scaffold extracts were added to continue culture. Wound closure was monitored and imaged under an optical microscope at 12-hour intervals.

2.5.2. Cell migration assay

To evaluate the effect of scaffolds on rRMEC migration, scaffold extracts (PH/GO-0 and PH/GO-1) were added to the lower chamber of a transwell system. The rRMECs (2×10^4 cells) were seeded into the upper chamber and incubated for 24 h. Migrated cells were fixed, stained with 0.1 % (w/v) crystal violet, washed with PBS, and imaged under an optical microscope. Migrated cell counts were quantified using ImageJ software.

2.5.3. Tube formation assay

To assess the angiogenic potential of scaffolds, 24-well plates were pre-coated with Matrigel. The rRMECs (8×10^4 cells) were seeded onto the Matrigel and cultured with PH/GO-0 and PH/GO-1 scaffold extract medium. Tube formation was observed and imaged at 12 h using an optical microscope. Quantitative analysis of vascular network parameters (e.g., branch, junction and node) was performed with ImageJ software [22].

2.5.4. The whole transcriptome analysis

To further examine the angiogenic capability of scaffolds, we performed cell transcriptomics analysis on both the rRMECs (control) and the rRMECs co-cultured with PH/GO-1 scaffold extract medium (PH/GO-1). RNA extraction, mRNA library construction, and sequencing were performed as previously reported [23]. RNA sequencing was conducted on the Illumina NovaSeq X plus platform. Principal component analysis (PCA) was conducted to enable the visualization of global sample patterns and detect inherent biological clusters. The DESeq2 package was used for differential expression analysis, with the significance criteria for differential expression set as a p-value <0.05 and an absolute log2 fold change >1.00. Volcano plots were generated with ggplot2 package to graphically display differential expression genes between groups. For functional annotations, Gene Ontology and Kyoto Encyclopedia of Genes and Genomes (KEGG) enrichment analysis, the topGO package and the clusterProfiler package were applied to identify and visualize key regulatory pathways among the DEGs respectively, with a p-value <0.05. The clusterProfiler package were also applied for gene set enrichment analysis (GSEA).

2.6. In vitro osteogenic evaluation

2.6.1. Alkaline phosphatase (ALP) staining

The rBMSCs were seeded into 24-well plates at a density of 1×10^4 cells per well. After 24 h of incubation, the culture medium was replaced with osteogenic induction medium extracted from PH/GO-0 and PH/GO-1 scaffolds. The medium was refreshed every other day. On days 7 and 14, the medium was removed, and cells were washed three times with PBS, followed by fixation with 4 % paraformaldehyde for 15 min. ALP staining was performed according to the instructions of the BCIP/NBT ALP Chromogenic Kit (Beyotime, China). After washing, stained cells were observed and imaged under an optical microscope.

2.6.2. Alizarin red s (ARS) staining

The rBMSCs were seeded into 24-well plates at 1×10^4 cells/well. After 24 h, the medium was replaced with osteogenic induction medium extracted from PH/GO-0 and PH/GO-1 scaffolds, and replenished every other day [24]. On days 14 and 21, the medium was discarded, cells were washed three times with PBS, and fixed with 4 % paraformaldehyde for 15 min. Subsequently, 500 μl of ARS staining solution (Beyotime, China) was added to each well and incubated in the dark for 5 min. After thorough rinsing, mineralized nodules were visualized and photographed under an optical microscope. For quantitative analysis, 10 % cetylpyridinium chloride solution was added to each well, incubated at 37 °C for 30 min, and the absorbance of the solubilized dye was measured at 562 nm using a microplate reader.

2.6.3. Western blotting analysis

The rRMECs were cultured with scaffold extracted medium for 3 days, while rBMSCs were cultured for 7 days in osteogenic induction medium extracted from scaffolds. After the culture period, total proteins were extracted using RIPA lysis buffer. Protein concentrations were quantified using a BCA Protein Assay Kit (Beyotime, China), followed by separation via SDS-PAGE with 20 μg of total protein loaded per lane. Proteins were transferred onto PVDF membranes, blocked with 5 % skim milk for 2 h at room temperature, and incubated with primary antibodies overnight at 4 °C under gentle shaking. After washing three times with Tris-buffered saline containing Tween-20 (TBST), membranes were incubated with horseradish peroxidase (HRP)-conjugated secondary antibodies for 1 h at room temperature. Protein bands were detected using an enhanced chemiluminescence (ECL) kit. For rRMECs, the detected proteins included platelet-derived growth factor receptor-beta (PDGF-β), hypoxia-inducible factor 1-alpha (HIF-1α), cluster of differentiation 31 (CD31), vascular endothelial growth factor receptor (VEGFA), and actin. For rBMSCs, the detected proteins included collagen type I alpha (COL1A1), runt-related transcription factor 2 (Runx2), osteocalcin (OCN), osteopontin (OPN), and actin.

2.7. In vivo osteogenic evaluation

2.7.1. Animal model of calvarial defect in SD rats

A total of 18 male Sprague-Dawley (SD) rats (8–10 weeks old) were used in this study. The rats were randomly divided into 3 groups ($n = 3$ per group): control group (blank defect), PH/GO-0 group, and PH/GO-1 group. During the surgery, the rats were anesthetized via intramuscular injection of tiletamine-zolazepam at 40 mg/kg and xylazine hydrochloride at 5 mg/kg. After anesthesia, the scalp was shaved and disinfected. A midline incision (~1.5 cm) was made along the skull using a surgical blade, and layers of skin and periosteum were dissected to expose the calvarium. Bilateral circular bone defects (5 mm in diameter) were created on the skull using a trephine drill, with continuous cooling saline irrigation to prevent thermal damage. Sterilized scaffolds (5 mm in diameter, 0.7 mm in thickness) were implanted into the defects. Postoperatively, the periosteum and skin were sutured. Rats received daily intramuscular injections of penicillin (50,000 IU/day) for infection prophylaxis. At 8 and 12 weeks post implantation, samples were harvested, fixed in 4 % paraformaldehyde, and analyzed by micro-computed tomography (Micro-CT) to quantify parameters of bone regeneration. Decalcified bone tissues were paraffin-embedded, sectioned, and subjected to hematoxylin and eosin (H&E) and Masson's trichrome staining for histological evaluation. Animal experiments were reviewed and approved by the Ethics Committee of Fudan University (No. 2024-DWYY-038).

2.7.2. Immunofluorescence

Tissue samples were fixed in 4 % paraformaldehyde, permeabilized, and blocked with PBS containing 5 % bovine serum albumin (BSA) to

prevent nonspecific binding. The samples were incubated with the primary antibody overnight at 4 °C to detect angiogenesis-related antibodies (VEGF, α-SMA) and osteogenesis-related antibodies (OCN, OPN). After PBS washing, samples were incubated with fluorescence-conjugated secondary antibodies for 1 h at room temperature. Unbound antibodies were removed by PBS washing, and nuclei were counterstained with DAPI. Sections were mounted with anti-fade medium and imaged under a Laser Scanning Confocal Microscope.

2.8. Statistical analysis

Data are expressed as mean ± standard deviation (SD). One-way analysis of variance (ANOVA) followed by Tukey's post hoc test was used for multiple comparisons. Statistical significance was defined as $p < 0.05$, with symbols: * for $p < 0.05$, ** for $p < 0.01$, and *** for $p < 0.001$.

3. Results and discussion

3.1. Preparation and characterization of PH/GO composite scaffold

The fabrication process of PH/GO composite scaffolds is shown in Fig. 1. First, PCL and HAp are mixed as the printing ink to construct the PH framework with a defined pore architecture via 3D printing. Concurrently, GO is uniformly dispersed into GEL solution. Subsequently, the GO/GEL solution is cast into the pores of the 3D-printed PH framework. Finally, the entire composite construct is subjected to freeze-drying and EDC/NHS cross-linking to obtain the final PH/GO composite scaffold, which possesses a multi-phase structure and good stability. Fig. 2A presents the macroscopic morphology of the scaffold, with the GEL matrix exhibiting a gradual darkening in color as the GO content increases (0 % to 2 %). SEM images in Fig. 2B further elucidated the microstructure of the composite scaffold (Fig. 2B1-3). The GEL matrix displayed a well-interconnected porous structure (Fig. 2B4-B6), optimized for cell infiltration, nutrient diffusion, and proliferation. Furthermore, successful integration of GO is observed in both the PH/GO-1 and PH/GO-2 groups, confirming the good interfacial compatibility between GO and the GEL matrix. Meanwhile, Figs. 2B7-B9 showed that the GEL/GO matrix effectively filled the macroscopic pores of the PH framework, and the two components were physically well-bonded without obvious delamination or detachment. In addition, high magnification observation of the surface of the PH framework further confirmed that the HAp nanoparticles were uniformly dispersed and embedded in the PCL matrix without obvious particle agglomeration (Fig. 2B10-B12). These morphological features laid a structural foundation for the composite scaffold to realize subsequent biological functions.

The incorporation of the GEL matrix significantly enhanced the scaffold's hydrophilicity. Hydrophilicity tests revealed that all scaffold groups exhibited favorable hydrophilic properties, with water droplets being completely absorbed within 8 s (Fig. 3A). The water absorption rates across groups were comparable, approximately 60 % (Fig. 3B). Additionally, the introduction of the GEL matrix induced the scaffold porosity to ~40 % in all groups, which is conducive to cell adhesion and infiltration (Fig. 3C). Thermal stability analysis further confirmed the scaffold's physical stability. As shown in Figs. 3D and 3E, TGA and DTG demonstrated excellent thermal stability across all scaffold groups, with significant mass loss observed only at ~400 °C, indicating sufficient thermal stability for biomedical implantation. Fourier-transform infrared (FTIR) spectroscopy revealed characteristic absorption peaks near 1620 cm^{-1} for the PH/GO-1 and PH/GO-2 groups, confirming successful GO integration into the scaffolds (Fig. 3F). All composite scaffolds exhibited excellent hemocompatibility, with hemolysis rates below 0.04 %, meeting national standards for blood-contacting

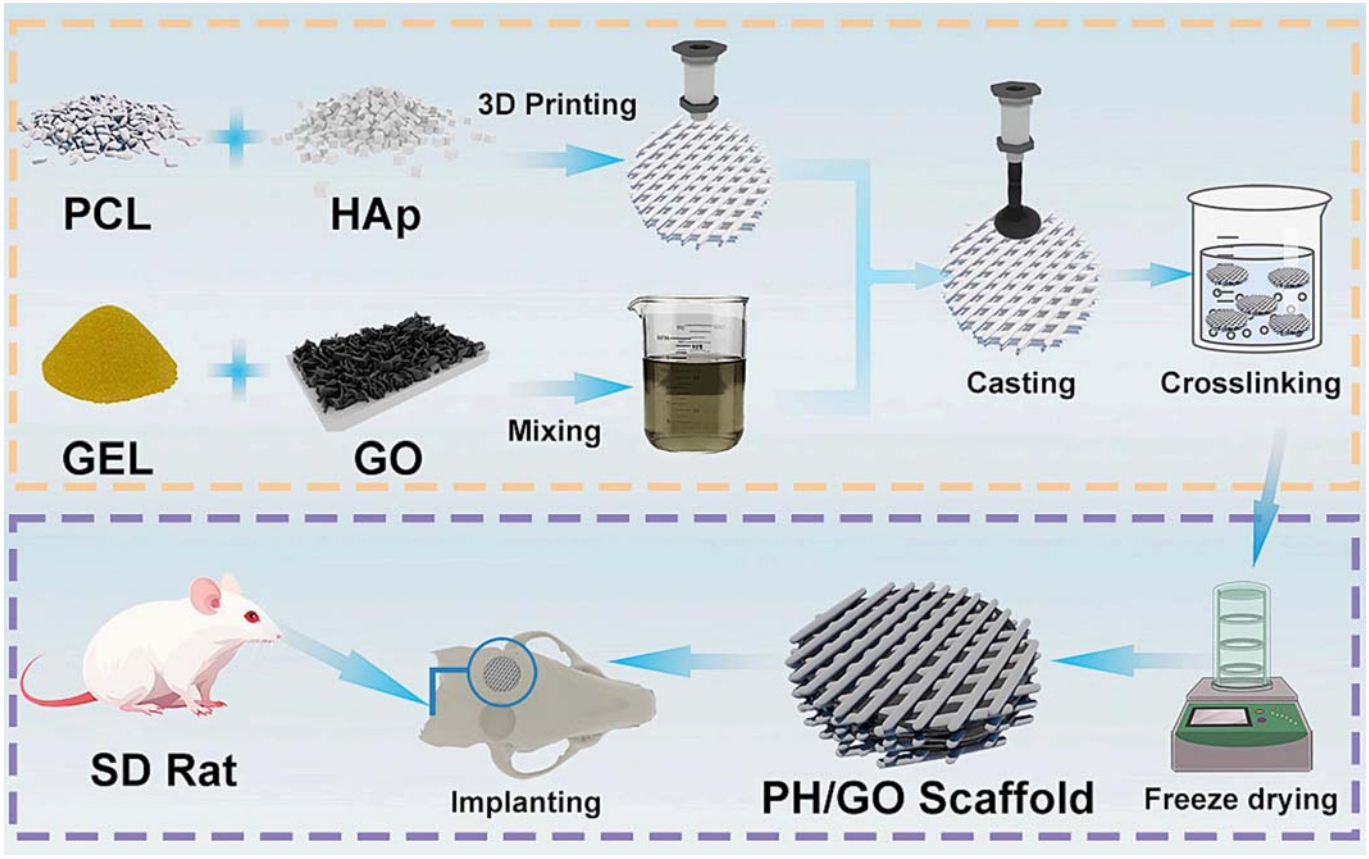

Fig. 1. Schematic illustration of 3D printing process for PH/GO composite scaffolds designed for sequential release of pro-angiogenic and osteoinductive factors.

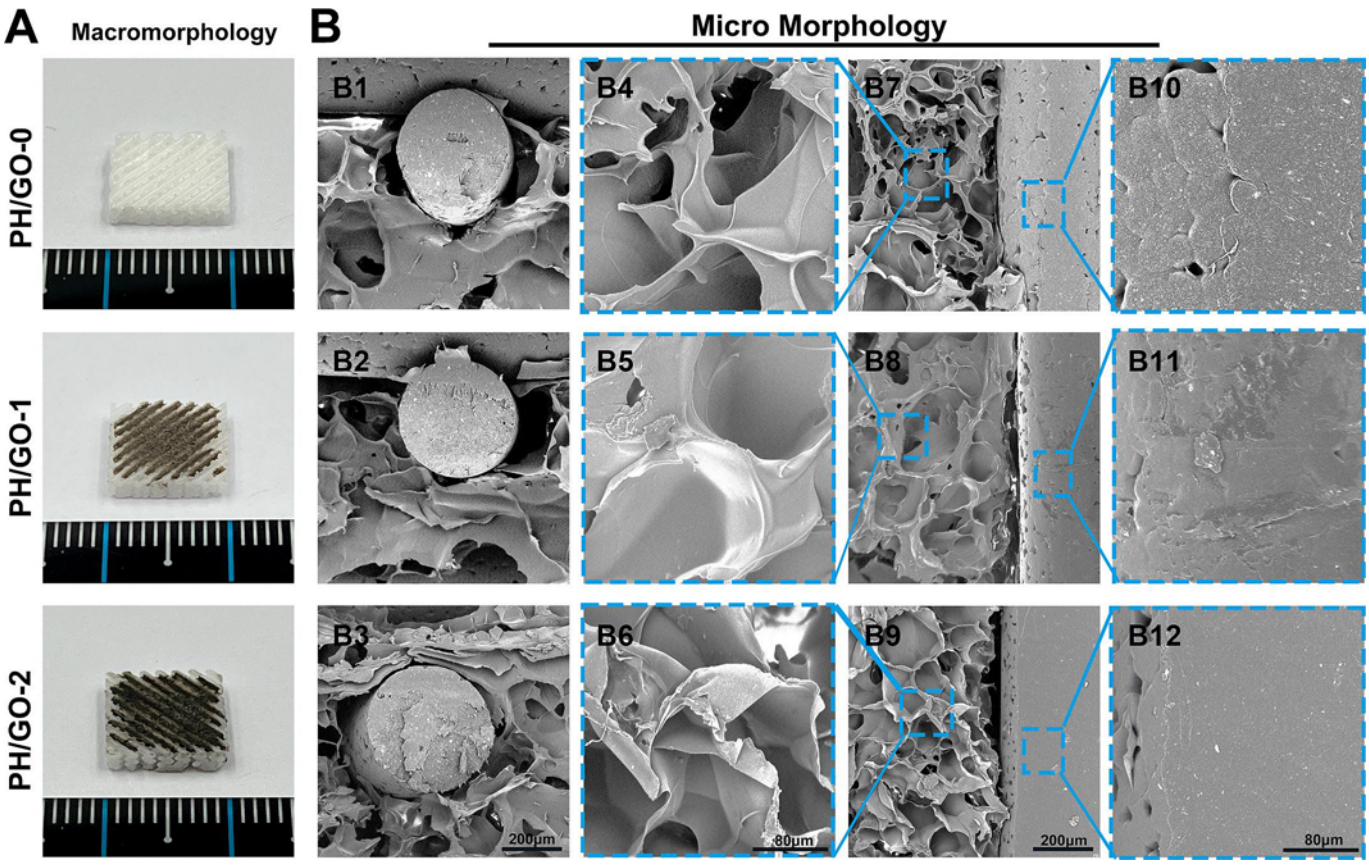

Fig. 2. Structural and morphological characterization of PH/GO composite scaffold. (A) Macroscopic photographs of PH/GO-0, PH/GO-1, and PH/GO-2 composite scaffolds. (B) SEM images: (B1–B3) Cross-sectional SEM images; (B7-B9) Surface SEM images; (B4-B6) SEM images of cast GEL within scaffolds; (B10-B12) SEM images of pH frameworks.

materials (Fig. 3G, Fig. S1) [25]. All groups exhibited a stable increased degradation rate, with degrading approximately 10 % by day 90 (Fig. 3H). In addition, macroscopic photographs showed that no significant degradation of the PH framework was observed over seven days, but the casting portion produced some degree of disintegration (Fig. S2). This suggests that GO may be able to be released rapidly at the initial stage due to faster degradation, effectively realizing the goal of rapid promotion of neovascularization at the initial stage. Ion release experiments demonstrated sustained calcium (Ca^{2+}) ion release from all scaffolds throughout the testing period (Fig. 3I), suggesting continuous stimulation of osteogenesis during bone repair. Mechanical testing confirmed that the PCL framework provided stable structural support. Stress–strain curves (Fig. 3J) revealed favorable mechanical properties for both GEL-cast and non-cast scaffolds. The compressive modulus (5.40 ± 0.37 MPa) and maximum compressive stress (13.62 ± 1.79 MPa) of cast scaffolds were slightly higher than those of non-cast scaffolds (4.74 ± 0.54 MPa and 11.97 ± 0.88 MPa, respectively), though the differences were not statistically significant (Fig. 3K, L). These results preliminarily validate the temporal release strategy for bioactive components in this study.

3.2. Cytocompatibility of PH/GO composite scaffold

GO holds broad biomedical potential due to its unique two-dimensional lamellar structure and physicochemical properties. However, its sharp edges may induce mechanical damage to cell membranes, potentially triggering cytotoxic responses. To mitigate these adverse effects, encapsulating GO within a GEL matrix represents a viable strategy. As a hydrolyzed product of natural collagen, GEL exhibits excellent biocompatibility and hydrophilicity, providing a favorable microenvironment for cell adhesion and spreading. The embedding of GO within the GEL matrix effectively shields its sharp edges, reducing direct contact with cell membranes and thereby attenuating mechanical damage. In order to screen out the GO addition concentration that achieves the best balance between biosafety and functionality, this study further carried out cytocompatibility evaluation experiments (Fig. 4A) under different GO content conditions, which provides the basis for subsequent scaffold optimization and mechanism studies.

Cellular responses to the scaffolds were comprehensively assessed through live/dead staining, CCK-8 proliferation assays, and colony formation assays. rBMSCs or rRMECs were co-cultured with scaffold extracted medium of varying concentrations to observe proliferous changes. Live/dead staining (Fig. 4B) revealed dose-dependent of cytotoxicity of GO toward both rBMSCs and rRMECs, with rRMECs exhibiting lower sensitivity to GO toxicity compared to rBMSCs. Consistent results were observed in CCK-8 proliferation assays (Fig. 4C, D) and colony formation assays (Fig. 4E-G), demonstrating inhibitory effects of high GO concentrations on early-stage cell proliferation. Notably, although the CCK-8 assay (Fig. 4C, D) showed that cell proliferation in the PH/GO-2 group appeared to recover after day 3, its significant proliferation inhibition in the early stage of culture and the evident cytotoxicity revealed by live/dead staining (Fig. 4A) cannot be overlooked. The early stage of bone repair is highly sensitive to changes in the microenvironment; even if this “early cytotoxicity” is only temporary, it may severely impair the critical functions of cells, thereby delaying or disrupting the subsequent regenerative cascade. Furthermore, combined with literature reports and the cytocompatibility data of this study, 1 % GO concentration was confirmed to achieve the optimal balance between bioactivity and safety [26]. Based on comprehensive cytocompatibility analysis, PH/GO-0 and PH/GO-1

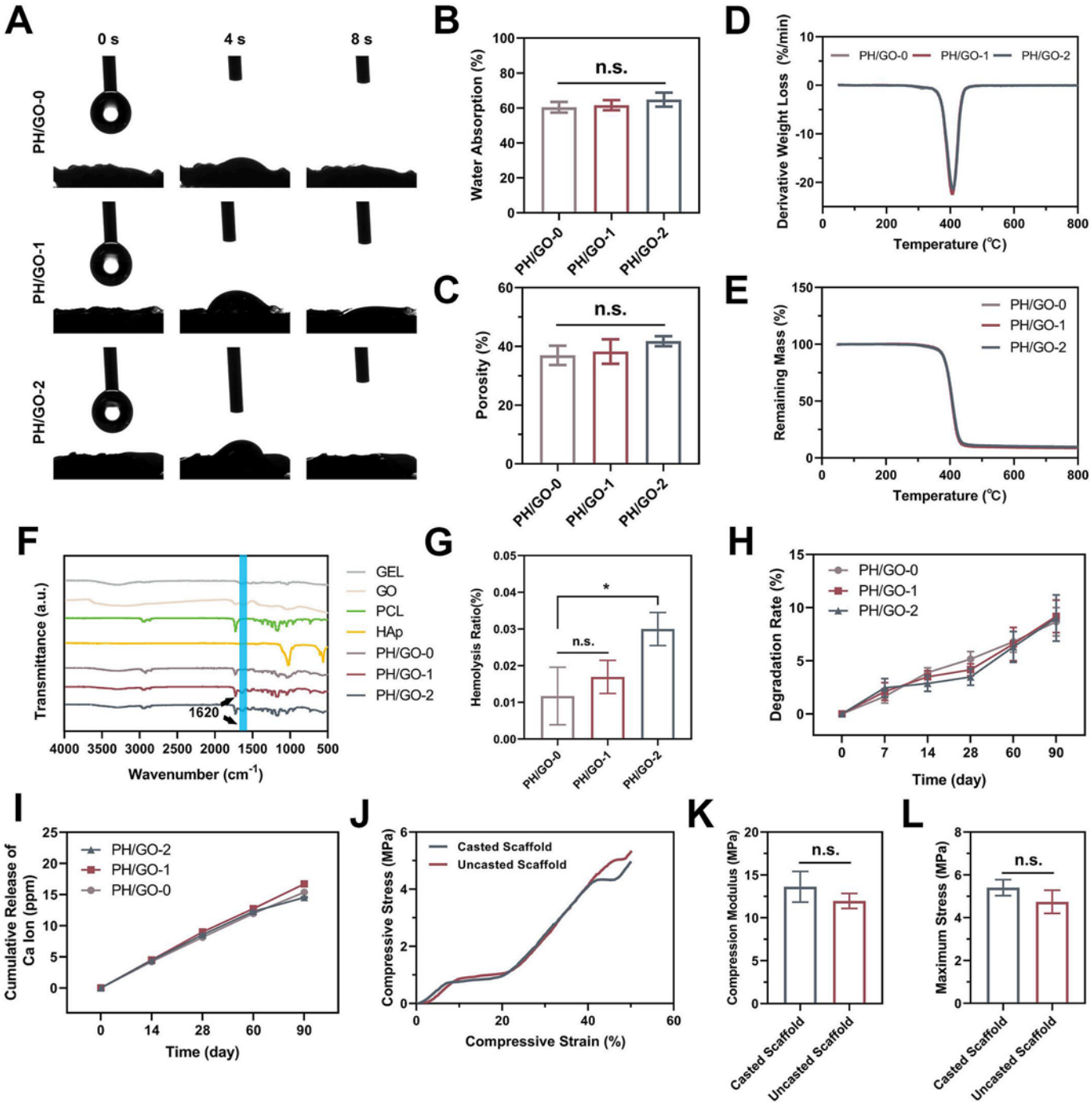

Fig. 3. Physicochemical characterization of composite scaffolds. (A) Water contact angle analysis. (B)Water absorption rate. (C) Porosity analysis. (D) Thermogravimetric analysis (TGA). (E) Derivative thermogravimetric (DTG) curves. (F) Fourier transform infrared (FTIR) spectroscopy. (G) Hemolysis ratio. (H) Degradation rate. (I) Ion release kinetics. (J) Stress–strain curves of cast vs. non-cast scaffolds. (K) Compressive modulus. (L) Maximum compressive strength. Means ± SD, n = 3. * $p < 0.05$.

scaffolds were selected for subsequent angiogenesis and osteogenesis studies to minimize potential cytotoxicity while ensuring experimental reliability.

3.3. *In vitro angiogenesis promotion ability of PH/GO composite scaffold*

Vascular endothelial cells are the main components of the vascular wall and play a crucial role in the process of angiogenesis. Their main functions include promoting the formation of new blood vessels and maintaining the stability of the vascular internal environment. We used rRMECs for evaluating the angiogenesis promotion ability of the composite scaffold with various experiments (Fig. 5A). During angiogenesis, the migration ability of endothelial cells is an important indicator of their functionality. Stronger migratory ability enables cells to rapidly respond to injury and cytokine stimulation, facilitating the construction of functional vascular networks in damaged areas [27]. Transwell migration assays (Fig. 5B, C) and scratch assays (Fig. 5D, E) were employed to quantitatively evaluate the effects of different scaffold material groups on the migratory capacity of rRMECs. The results demonstrated that, compared to the control group and PH/GO-0, PH/

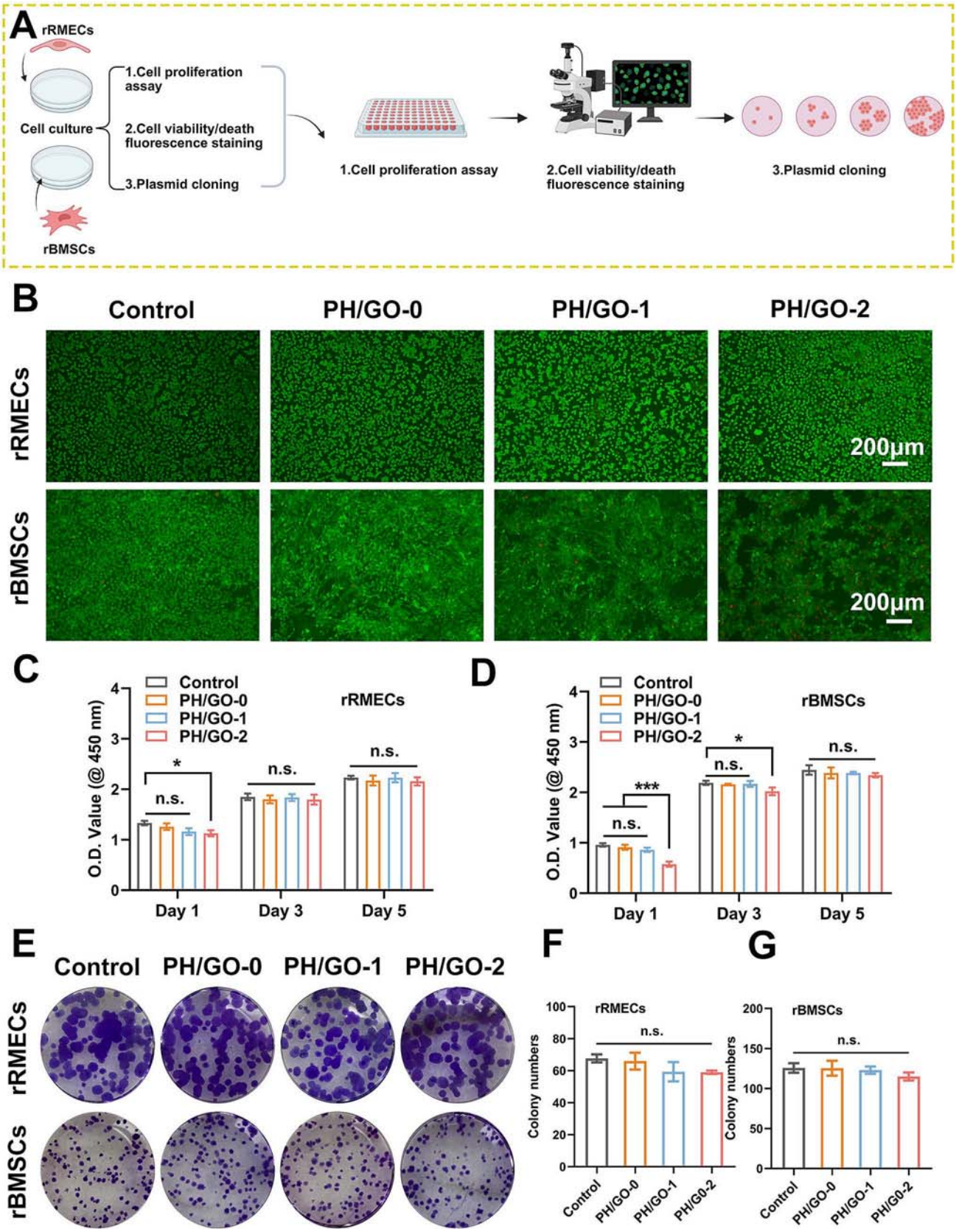

Fig. 4. *In vitro* biocompatibility evaluation of PH/GO scaffold. (A) Schematic workflow for evaluation of scaffolds' cytocompatibility. (B) Live/dead staining at day 3. Bars = 200 μm. (C, D) CCK-8 assay for proliferation activity of rRMECs and rBMSCs at days 1, 3, and 5. (E) Colony formation staining at day 7. (F, G) Quantitative analysis of colony formation. Means ± SD, n = 3. * $p < 0.05$, *** $p < 0.001$.

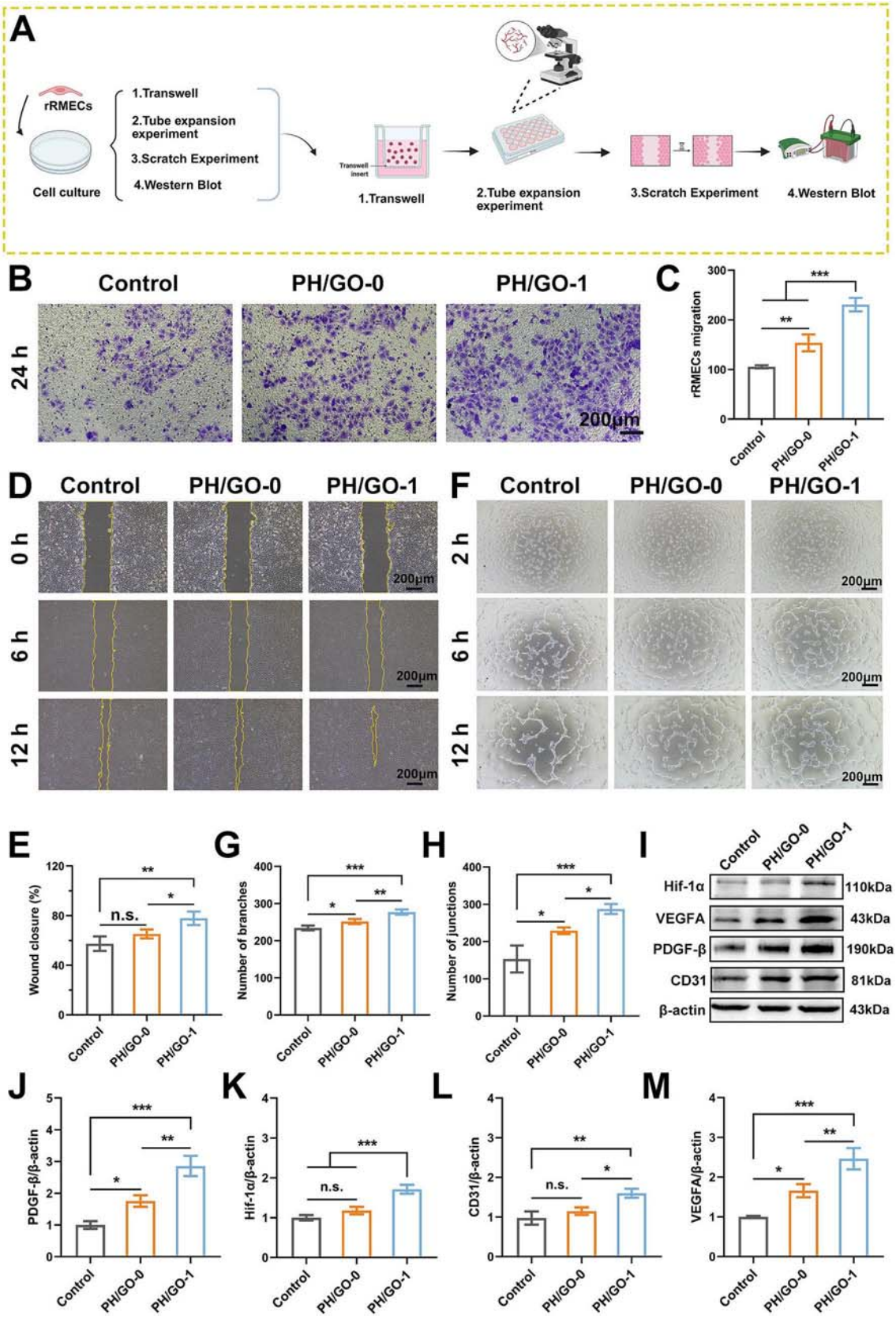

Fig. 5. *In vitro* angiogenic inductive potential of PH/GO scaffold. (A) Experimental workflow for evaluation of scaffolds' angiogenesis promotion ability. (B) Transwell migration assay of rRMECs treated with PH/GO-0 and PH/GO-1. (C) Quantitative analysis of migrated cells. (D) Scratch healing assay at 0, 6, and 12 h. (E) Quantified wound healing area. (F) Tubular structure formation by rRMECs at 2, 6, and 12 h. (G, H) Quantitative analysis of vascular network parameters at 6 h (branch points and junctions). (I) Western blot analysis of angiogenesis-related proteins. (J-M) Quantitative analysis of protein expression levels. Bars = 200 μm. Means ± SD, n = 3. * $p < 0.05$, ** $p < 0.01$, *** $p < 0.001$.

GO-1 significantly enhanced cell migration, further validating the significant advantage of PH/GO-1 in promoting endothelial cell migration.

To further evaluate the impact of PH/GO scaffold on angiogenesis, we conducted tube formation assays. The results demonstrated that the PH/GO-1 group exhibited significantly more vascular branches and interconnected tubular structures at the 2-, 6- and 12-hour time points, with peak tube-forming capacity observed at 6-hour (Fig. 5F). Quantitative analysis revealed that the PH/GO-1 induced 277 ± 6.93 branch points and 287 ± 13.43 junctions, significantly higher than the control and PH/GO-0 groups (Fig. 5G, H). These findings indicate that PH/GO-1 not only enhances endothelial cell migration but also significantly promotes vascular network formation during angiogenesis. PH/GO-1 may facilitate rapid assembly and stabilization of vascular structures by improving endothelial cell adhesion and migratory capacity.

To investigate the molecular regulatory mechanisms of PH/GO scaffold in angiogenesis, we examined the expression levels of key angiogenesis-related proteins, including HIF-1α, VEGFA, PDGFR-β, and CD31 (Fig. 5I) [28,29]. HIF-1α serves as an initiating signal for angiogenesis by activating downstream angiogenesis-related gene expression in hypoxic microenvironments. Studies have demonstrated that HIF-1α directly regulates VEGFA, a key effector molecule of vascular neogenesis. VEGFA promotes endothelial cell proliferation and migration,

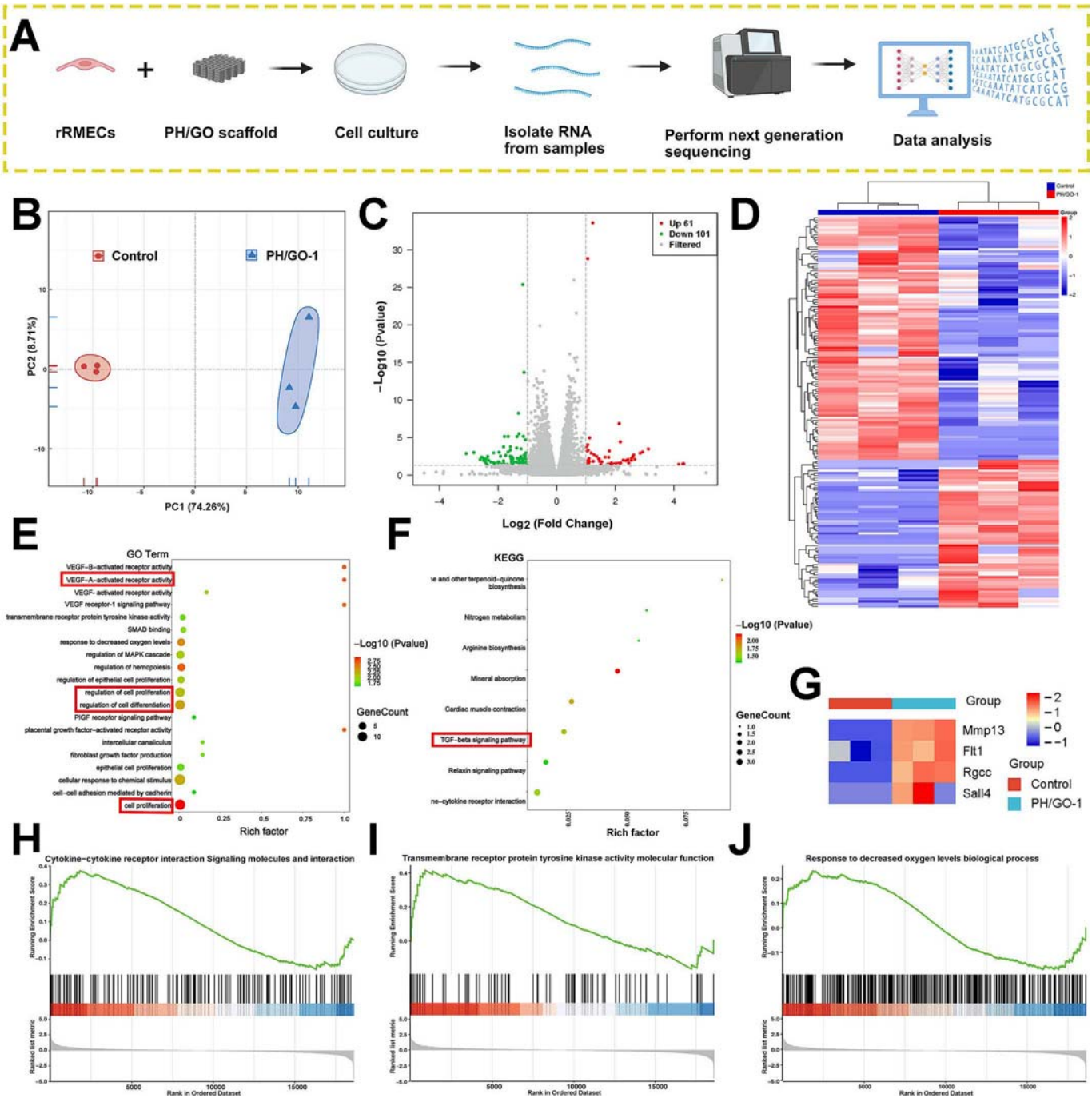

Fig. 6. Transcriptome RNA sequencing analysis of the PH/GO-1 group vs control group. (A) Schematic workflow for transcriptomic analysis. (B) Principal component analysis (PCA) plot. (C) Volcano plot and (D) Heatmap of differentially expressed genes. (E) Gene Ontology and (F) KEGG enrichment analysis showed upregulated pathways in PH/GO-1. (G) Heatmap of the angiogenesis-related differentially expressed genes in PH/GO-1. (H-J) GSEA showed upregulated pathways in PH/GO-1.

thereby facilitating the formation of neovascular networks. PDGFR-β, activated by binding to PDGF-BB, is a regulator of vascular maturation, which recruits pericytes to wrap around the neovasculature and promotes vascular stabilization. And CD31 is a marker of endothelial cell function and vascular integrity. Our results showed that the PH/GO-1 group exhibited significantly higher expression levels of HIF-1α, VEGFA, PDGFR-β, and CD31 compared to the control and PH/GO-0 groups (Fig. 5J–M). In addition, we noted that there was no significant difference in the expression of HIF-1α and CD31 between the PH/GO-0 group and the control group (Fig. 5K, L). These data suggested that PH/GO-1 enhanced early-stage angiogenesis by activating the HIF-1α-VEGFA signaling pathway [30]. Concurrently, the upregulation of PDGFR-β and CD31 promoted vascular maturation and stabilization. Specifically, the rapid release of GO from the PH/GO-1 scaffold significantly upregulates pro-angiogenic factors, supporting the entire process of angiogenesis. This indicates the preliminary success of our strategy to design a time-sequential release scaffold.

To further investigate the potential regulatory mechanisms of the composite scaffold in angiogenesis, transcriptomic sequencing analysis was performed on the PH/GO-1 and control groups (Fig. 6A). The principal component analysis (PCA) plot (Fig. 6B) revealed that samples formed two distinct clusters, confirming significant differences between groups. This provides a solid foundation for subsequent differential expressed genes and functional pathway enrichment analysis. A total of 162 differentially expressed genes (DEGs) were identified, with 61 genes upregulated and 101 downregulated in the PH/GO-1 group (Fig. 6C, D). The results revealed that several upregulated genes participate in vascular formation processes (Fig. 6G), indicating that PH/GO-1 possesses a significant advantage in promoting neovascularization. Upregulation of Fms related receptor tyrosine kinase 1 (FLT1, also known as VEGFR-1), a receptor for VEGF, activates the PI3K/PIK3R1 signaling pathway, initiating downstream cascades that promote vascular endothelial cell behavior and vascular network construction [31]. Additionally, regulator of cell cycle (RGCC), a key regulatory gene in cell cycle progression, can be activated via the HIF-1α/VEGF pathway in response to hypoxic stimuli, mediating smooth muscle cell migration and neointima formation [32]. Spalt-like protein 4 (SALL4) directly binds to the promoter regions of VEGF-A, -B, and -C, enhancing their transcriptional expression, thereby boosting endothelial cell proliferation, migration, and tube formation capacity [33]. Concurrently, the upregulation of Matrix Metalloproteinase 13 (MMP-13) suggests the scaffold may amplify the angiogenic effect by modulating the FAK/ERK signaling axis to synergistically stimulate VEGF-A secretion from fibroblasts and endothelial cells [34].

Based on Gene Ontology enrichment analysis (Fig. 6E), DEGs in the PH/GO-1 group were significantly enriched in vascularization-related biological processes, including cell proliferation, VEGFR1 signaling pathway, and VEGF-A-activated receptor activity, indicating that this scaffold drives endothelial cell migration and proliferation through the VEGF/VEGFR signaling axis, possessing molecular regulatory capabilities for inducing angiogenesis [35]. KEGG pathway analysis (Fig. 6F) further revealed enhanced activity in the TGF-β/SMAD signaling pathway, which promotes angiogenesis by inducing VEGF expression via SMAD2-mediated signaling while enhancing vascular wall integrity and intimal tissue accumulation [36]. Simultaneously, although HIF−1α transcription levels showed no significant changes in the microenvironment of decreased oxygen, its target genes were generally upregulated, suggesting that the scaffold may enhance hypoxic response by improving post-transcriptional stability [37]. GSEA (Fig. 6H–J) confirmed upregulation of cytokine-receptor interactions and hypoxia response pathways, where chemokine CXCL12 facilitates directed migration of endothelial progenitor cells to hypoxic regions [38]. Notably, receptor tyrosine kinases (RTKs) such as VEGFRs and PDGFRs play central roles in vascular remodeling by regulating cell growth, migration, and differentiation. Under hypoxic conditions, HIF-1α pathway activation stabilizes HIF-1α by inhibiting prolyl hydroxylase activity, thereby initiating transcription of pro-angiogenic genes including VEGF and PDGF. These signals are transmitted through RTKs (e.g., VEGFR, PDGFR), ultimately driving neovascularization [39]. Collectively, these Gene Ontology, KEGG, and GSEA enrichment analyses elucidate the complete mechanism by which the PH/GO-1 scaffold promotes angiogenesis through synergistic effects across multiple pathways (Fig. S3). The combined action of these mechanisms establishes a solid molecular foundation for the early vascularization of this composite scaffold in bone defect repair, highlighting its significant value in remodeling the defect microenvironment and enhancing its functionality. Moreover, it is notable that a significant up-regulation of HIF-1α protein level was observed in PH/GO-1 group, whereas its mRNA abundance showed no significant change. This phenomenon is consistent with the classical regulatory mechanism of HIF-1α, which is primarily controlled at the post-translational level rather than at the transcriptional level. It is speculated that the PH/GO-1 scaffold may stabilize HIF-1α protein by creating a local hypoxic microenvironment or by inhibiting prolyl hydroxylase activity through other mechanisms [40]. Furthermore, as reported in the literature, enhanced mRNA stability or increased translational efficiency mediated by RNA-binding proteins (such as HuR) may also synergistically contribute to this process [41]. This rapid accumulation of HIF-1α protein, driven by protein stability rather than an increase in mRNA, is sufficient to activate the expression of downstream angiogenic factors such as VEGF [42], which is fully consistent with the pro-angiogenic results observed in this study.

3.4. *In vitro osteogenic properties of PH/GO composite scaffold*

In bone tissue engineering, scaffold materials promote the differentiation of mesenchymal stem cells (MSCs) into osteogenic lineages by regulating extracellular matrix (ECM) secretion and cellular differentiation behavior, thereby effectively repairing bone defects. We used rBMSCs for evaluating the osteogenesis promotion ability of the composite scaffold with various experiments (Fig. 7A). ALP, a hallmark enzyme of osteoblast activation and differentiation, reflects the metabolic activity of osteoblasts and serves as a critical early-stage indicator in bone repair processes [43]. As shown in Fig. 7B, the PH/GO groups exhibited significantly higher ALP activity compared to the control group at both day 7 and day 14 of osteogenic induction. ARS staining was performed to assess calcium deposition (Fig. 7C). Results revealed no significant mineralization across groups at day 7, which might be due to the fact that matrix mineralization had not yet significantly initiated. However, by day 14 and 21, the PH/GO groups showed substantially more mineralized nodules compared to the control group. Quantitative analysis revealed that the absorbance value of PH/GO-1 at 562 nm was 2.01 ± 0.07, which was significantly higher than that of the control group (0.88 ± 0.09) and the PH/GO-0 group (1.63 ± 0.13) (Fig. 7D). These findings suggest that PH/GO scaffold not only promotes early osteogenic activation and differentiation but also significantly enhances calcium deposition and matrix mineralization. The improved mineralization capacity of PH/GO-1 may be attributed to GO-mediated facilitation of ECM formation and calcium deposition during matrix mineralization.

To explore the molecular mechanisms of PH/GO-induced osteogenic differentiation, the expression levels of key osteogenic markers were quantified (Fig. 7E). Compared to the control and PH/GO-0 groups, PH/GO-1 significantly upregulated the expression of Runx2, COL1A1, OCN, and OPN (Fig. 7F–I). These results indicated that PH/GO-1 promoted osteoblast activation and differentiation by enhancing the expression of osteogenesis-related proteins. The enhanced osteogenic differentiation of rBMSCs by PH/GO-1 is potentially mediated through Runx2 upregulation, a central transcriptional driver that activates downstream targets (e.g., COL1A1, OCN) essential for bone matrix synthesis and mineralization [44]. COL1A1 is a major component of type I collagen, which forms a fibrous network in the extracellular matrix and participates in the process of cell attachment and mineralization. Runx2

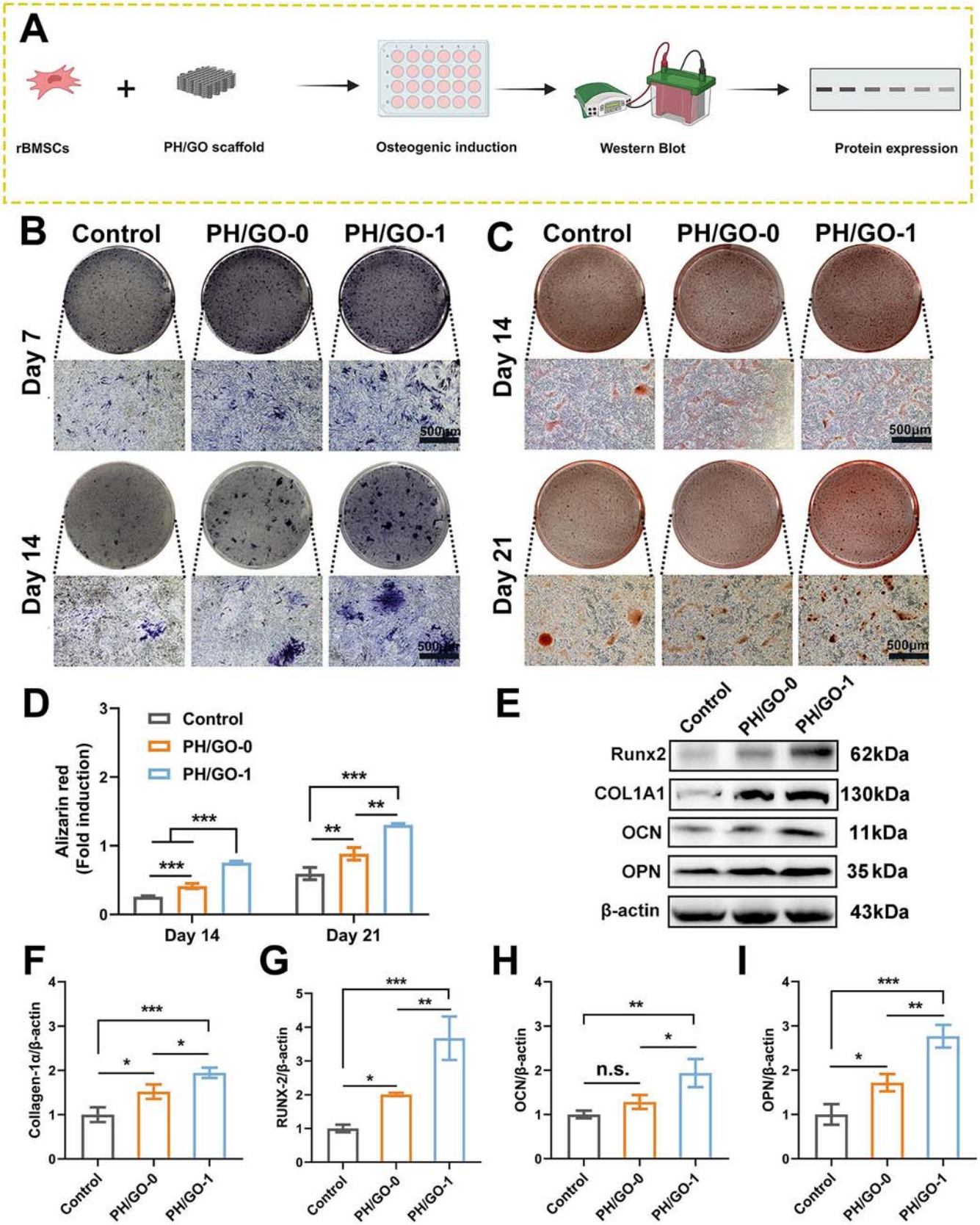

Fig. 7. *In vitro* osteogenic inductive capacity of PH/GO scaffold. (A) Experimental workflow for osteogenic differentiation assays. (B) ALP staining at days 7 and 14. (C) ARS staining at days 14 and 21. (D) Quantitative analysis of ARS staining. (E) Western blot detection of osteogenic markers (Runx2, COL1A1, OCN, and OPN). (F-I) Quantitative analysis of protein expression levels. Bars = 500 μm. Means ± SD, n = 3. * $p < 0.05$, ** $p < 0.01$, *** $p < 0.001$.

directly binds to the promoter of the COLLAGEN-1A gene and promotes its transcription. In our study, increased expression of Runx2 and COL1A1 may be related with the early stages of osteoblast differentiation following PH/GO-1 administration. On the other hand, the increase in the expression of OCN and OPN reflected the effects of PH/GO-1 on the positive effects of PH/GO-1 on the maturation and mineralization process of osteoblasts [45]. Furthermore, compared with the control group, the expression of Runx2, COL1A1 and OPN, except OCN in the PH/GO-0 group was significantly upregulated. This further indicates that GO may activate specific signaling pathways and significantly promote the osteogenic differentiation process of rBMSCs.

3.5. In vivo bone regeneration evaluation of PH/GO composite scaffold

To further validate the *in vivo* osteogenic capacity of the PH/GO scaffold, we established a calvarial defect model in SD rats and implanted the scaffolds into the defect sites (Fig. S4) and conducted following experiments (Fig. 8A). At week 8 and 12 post-operation, micro-CT and histological staining techniques were employed to evaluate new bone formation. Micro-CT analysis demonstrated that the PH/GO-1 group outperformed the control group at all time points (Fig. 8B). At week 8, PH/GO-1 exhibited a larger area of new bone coverage compared to both the control and PH/GO-0 groups. By week 12, new bone formation area in the PH/GO-1 group further increased, nearly filling the entire defect area, with a bone volume to tissue volume ratio (BV/TV) of 29.79 ± 2.7 %, significantly higher than the control group (Fig. 8D). Bone mineral density (BMD) analysis revealed that both PH/GO-0 and PH/GO-1 groups showed significantly elevated BMD levels compared to the control at 8 and 12 weeks (Fig. 8C). PH/GO-0 showed no statistically significant differences from the control in BV/TV, trabecular number (Tb.N), or trabecular thickness (Tb.Th) other than in BMD (Fig. S5). In contrast, PH/GO-1 demonstrated significantly superior values for all micro-CT parameters relative to the control, despite no intergroup differences in structure model index (SMI). Quantitative analysis via Micro-CT (Fig. 8C, D) confirmed the significant advantages of the PH/GO-1 group in terms of BV/TV and BMD. This excellent mineralization and new bone formation volume is a direct reflection of the success of the sequential release strategy for bioactive elements. The sustained release of Ca^{2+} ions from the PH scaffold framework provides the necessary material basis for bone matrix mineralization, which can be confirmed by the increased BMD of the PH/GO-0 group compared with the control group. However, there was no significant difference in BV/TV between the PH/GO-0 group and the control group (Fig. S5), which strongly indicates that osteogenic signals alone, without early vascularization, may be insufficient for bone defect repair. This highlights the core role of GO in the PH/GO-1 group: relying on the rapid degradation of GEL, GO is released in the early stage, rapidly initiating angiogenesis and providing a sufficient nutrient and oxygen environment for subsequent osteoblast migration, proliferation, and bone matrix deposition.

Histological analysis using hematoxylin-eosin (H&E) and Masson's trichrome staining (Fig. 8E) revealed limited new bone formation in the control group at 8 weeks, primarily confined to marginal regions, while the central defect area remained dominated by fibrous tissue. In contrast, both PH/GO-0 and PH/GO-1 groups displayed new bone tissue extending from the defect margins toward the center, with PH/GO-1 exhibiting greater collagen deposition than PH/GO-0 (Fig. S6). By week 12, scaffold degradation progressed, accompanied by significant new bone formation in scaffold groups. Notably, the PH/GO-1 group demonstrated near-complete defect closure with abundant new bone, whereas PH/GO-0 showed inferior osteogenesis. Histomorphological results further verified the positive effect of the PH/GO-1 group on osteogenesis. Masson staining showed a large amount of blue-stained collagen matrix in the PH/GO-1 group, whereas the control group and PH/GO-0 group mainly contained red-stained fibrous tissue. This significant collagen deposition may be an indirect effect of GO-induced early vascularization; that is, successful vascularization recruits more osteoblasts, thereby promoting more bone matrix deposition. Meanwhile, the trend of new bone extending from the edge to the center in H&E staining also confirms that this design provides ideal spatial channels for cell and vascular ingrowth. These findings suggest that the PH/GO-1 scaffold promotes superior bone regeneration, likely attributable to the sequential release of bioactive components that synergistically enhance bone repair.

3.6. In vivo PH/GO composite scaffold elevate VEGF/α-SMA and OCN/OPN levels

To elucidate the vascularization and osteogenesis mechanisms, angiogenesis (VEGF/α-SMA) and osteogenic markers (OCN/OPN) were analyzed via immunofluorescence at 8/12 weeks (Fig. 9A). PH/GO-1 group exhibited enhanced α-SMA (green) level localized to perivascular pericytes and VEGF (red) expression overlapping nascent capillaries (Fig. 9B). Quantitatively, PH/GO-1 group showed significantly higher α-SMA and VEGF levels than control and PH/GO-0 groups (Fig. 9C, D). Notably, PH/GO-0 displayed no elevation of VEGF versus control at 8 weeks, while PH/GO-1 sustained significant increases across both timepoints. This demonstrates that GO's sustained release in PH/GO-1 amplifies pro-angiogenic factor expression and neovascularization, establishing a regenerative niche for bone repair.

PH/GO-1 group also demonstrated dense OCN (red) and OPN (green) expression in new bone regions, with fluorescence intensities reaching 16.07 ± 1.43 % (OCN) and 18.57 ± 1.12 % (OPN) at 12 weeks, outperforming other groups (Fig. 9E, F). Although the OCN and OPN expression levels in the PH/GO-0 group were higher than those in the control group at both timepoints, they remained lower than those in the PH/GO-1 group. These results indicate that the PH framework can support bone repair in the defect area through the continuous release of Ca^{2+} ions, while the incorporation of GO release accelerate vascularization, thereby promoting the bone regeneration process.

In brief, the PH/GO composite scaffold achieves time-sequential controlled release of bioactive elements to address stage-specific biological requirements during bone repair. Early sustained release of GO enhances angiogenic factor expression, accelerating vascular network formation to facilitate nutrient supply and cell recruitment. The PH framework provides mechanical support while continuously releasing Ca^{2+} ions to promote osteoblast proliferation, differentiation, matrix mineralization, and bone remodeling. This strategy effectively coordinates vascularization and osteogenesis, culminating in comprehensive bone defect regeneration. Although favorable results have been achieved in both *in vitro* and *in vivo* experiments, this study still has the following limitations: The SD rat calvarial defect model employed in this study is a non-weight-bearing model, and its mechanical properties and repair efficacy need to be further verified in weight-bearing bone defects in subsequent research. Moreover, the long-term biosafety of GO still requires longer-duration *in vivo* degradation studies and systematic toxicological observations. For future research, we will focus on optimizing the degradation rate of the scaffold to match the mechanical requirements, and explore its application in larger animal models.

4. Conclusion

In this study, a PH/GO composite scaffold with a multiphase structure was successfully constructed by combining 3D printing and freeze-drying technology. The scaffold utilized the rapid degradation of GEL and the slow degradation of PCL to physically achieve the time-sequential release of two key active components. *In vitro* experiments confirmed that the GEL/GO component significantly activated the HIF-1α/VEGF signaling pathway at the early stage, promoting the migration and tube formation of rRMECs. In contrast, the PCL/HAp framework continuously released Ca^{2+}, effectively supporting the late osteogenesis and mineralization of rBMSCs. The results of the *In vivo* rat cranial defect

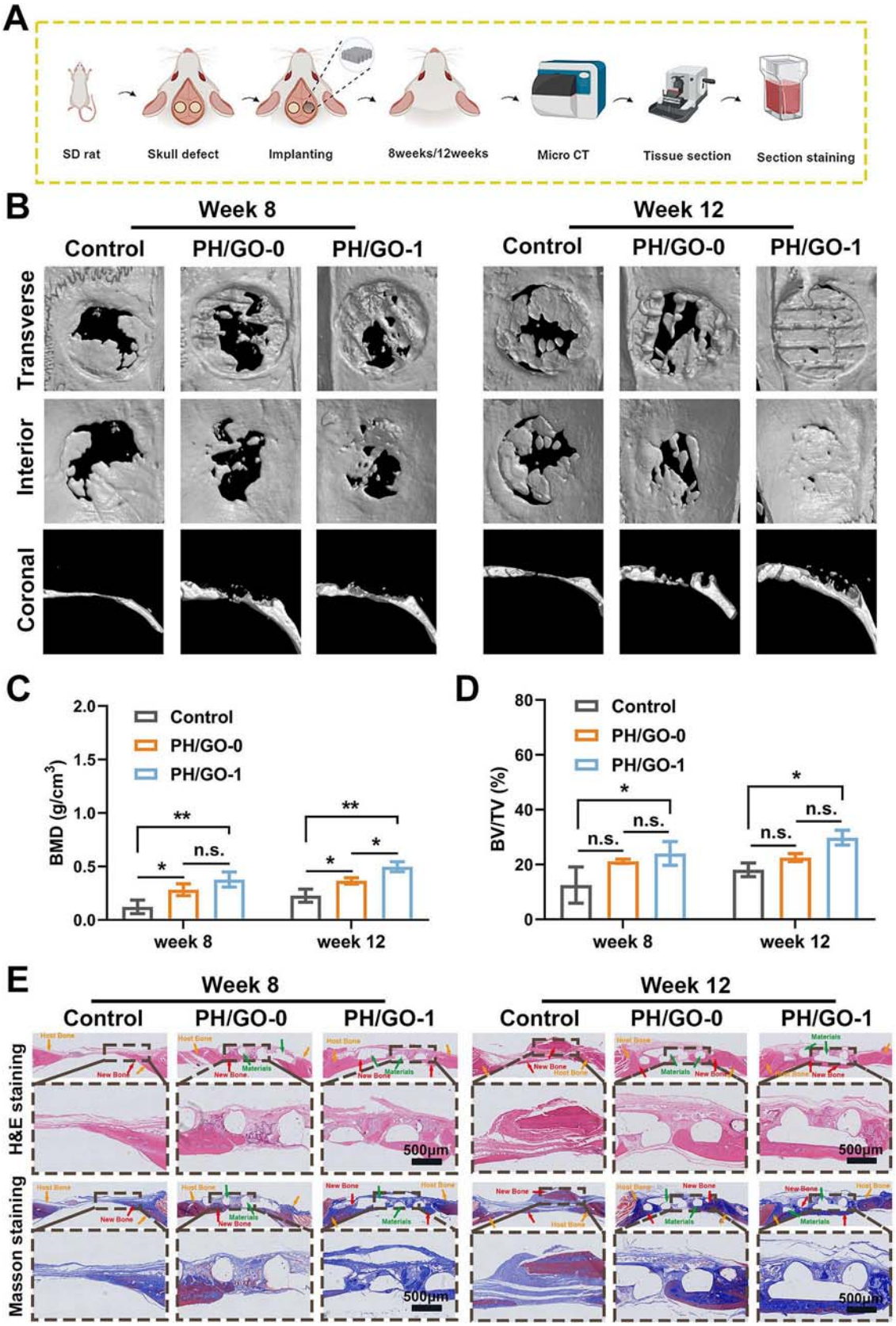

Fig. 8. *In vivo* osteogenic efficacy evaluation of PH/GO scaffold. (A) Schematic workflow of rat calvarial defect model establishment, scaffold implantation, and *in vivo* osteogenic efficacy evaluation. (B) 3D reconstructed micro-CT images at 8- and 12-weeks post-implantation. Quantitative assessment of (C) BMD and (D) BV/TV. (E) Histomorphological analysis via H&E and Masson's trichrome staining, Bars = 500 μm. Means ± SD, n = 3. * $p < 0.05$, ** $p < 0.01$.

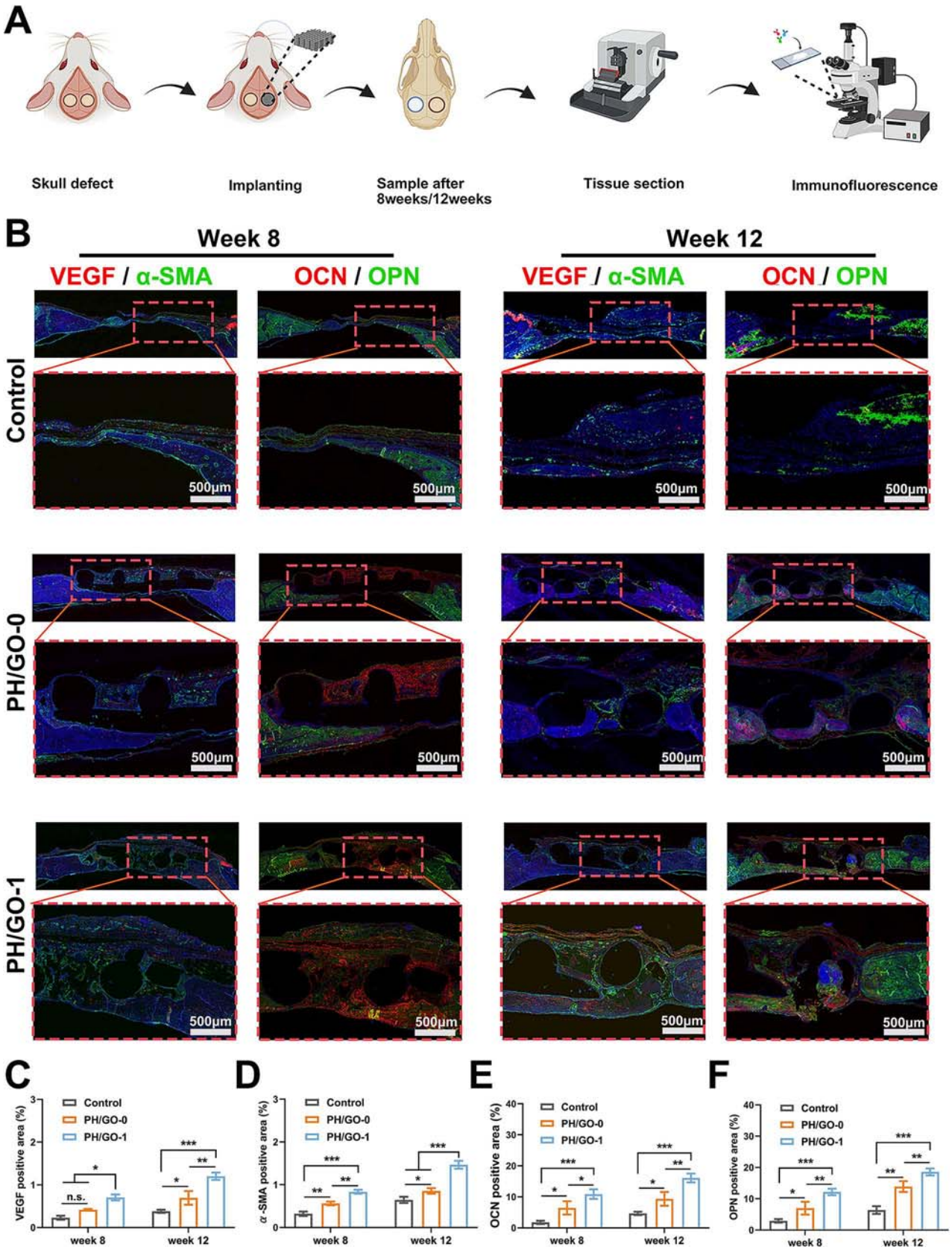

Fig. 9. The PH/GO composite scaffold confers dual angiogenic and osteogenic capabilities through elevated α-SMA-VEGF and OCN-OPN signaling. (A) Schematic workflow of rat calvarial defect model establishment, scaffold implantation, and IF stain. (B) Angiogenesis-related proteins (VEGF-red, α-SMA-green,) and osteogenesis-related proteins (OCN-red, OPN-green) were detected by IF at week 8 and 12. Bars = 500 μm. (C-F) Quantitative analysis of IF intensity for angiogenesis (α-SMA, VEGF) and osteogenesis (OCN, OPN) at 8 and 12 weeks. Means ± SD, n = 3. * $p < 0.05$, ** $p < 0.01$, *** $p < 0.001$. (For interpretation of the references to colour in this figure legend, the reader is referred to the web version of this article.)

model functionally validated the necessity of the time-series strategy. The PH/GO-1 group exhibited significant bone regeneration, and its 12-week new bone production was significantly higher than that of the other groups. This critical comparison demonstrates that early vascularization induced by GO is a prerequisite for the establishment of a regenerative microenvironment that supports the subsequent deposition of new bone matrix. In conclusion, this scaffold design with sequential release of active ingredients is an effective way to achieve synergistic enhancement of bone repair.

CRediT authorship contribution statement

Chunchun Li: Conceptualization, Methodology, Investigation, Formal analysis, Writing – original draft. **Cuiting Lyu:** Conceptualization, Methodology, Investigation, Formal analysis, Writing – original draft. **Yangfan Ding:** Conceptualization, Methodology, Investigation, Formal analysis, Writing – original draft. **Ziying Feng:** Investigation, Formal analysis, Data curation. **Jinzan Zhu:** Investigation, Formal analysis, Data curation. **Yichen Zhao:** Investigation, Formal analysis, Data curation. **Mohamed EL-Newehy:** Investigation, Formal analysis. **Meera Moydeen Abdulhameed:** Investigation, Formal analysis.. **Duyao Su:** Investigation, Formal analysis. **Pengfei Cai:** Conceptualization, Methodology, Writing – review & editing, Project administration. **Xiumei Mo:** Conceptualization, Methodology, Writing – review & editing, Project administration, Funding acquisition. **Liang Song:** Conceptualization, Methodology, Writing – review & editing, Project administration, Funding acquisition.

Declaration of competing interest

The authors declare that they have no known competing financial interests or personal relationships that could have appeared to influence the work reported in this paper.

Acknowledgements

This work was supported by Natural Science Research Funds of Minhang District, Shanghai (No. 2023MHZ015), Excellence Talent Cultivation Program of Shanghai Fifth People's Hospital, Fudan University (No. 2024WYRCZY01), Construction Project for Medical Specialties of Excellence in Minhang District, Specialty of Excellence A Class (2025MWTZA02), Natural Science Research Funds of Minhang District, Shanghai (No. 2024MHZ013), Scientific Research Project funded by Shanghai Fifth People's Hospital, Fudan University (No. 2020WYZT03), Science and Technology Commission of Shanghai Municipality, China (20DZ2254900), Sino German Science Foundation Research Exchange Center, China (M-0263). This project was also supported by Ongoing Research Funding program (ORF-2025-65), King Saud University, Riyadh, Saudi Arabia. Thanks to https://www.biorender.com for assisting in the creation of some of the figures in this article.

Appendix A. Supplementary data

Supplementary data to this article can be found online at https://doi.org/10.1016/j.matdes.2025.115273.

Data availability

Data will be made available on request.

References

[1] S. Singh, D.K. Sarma, V. Verma, R. Nagpal, M. Kumar, From cells to environment: exploring the interplay between factors shaping bone health and disease, Medicina (Kaunas) 59 (2023), https://doi.org/10.3390/medicina59091546.
[2] W. Li, Y. Wu, X. Zhang, T. Wu, K. Huang, B. Wang, J. Liao, Self-healing hydrogels for bone defect repair, RSC Adv. 13 (25) (2023) 16773–16788, https://doi.org/10.1039/d3ra01700a.
[3] P. He, Y. Zhao, B. Wang, G. Liu, L. Zhang, M. Li, B. Xu, W. Cai, C. Chu, Y. Cong, A biodegradable magnesium phosphate cement incorporating chitosan and rhBMP-2 designed for bone defect repair, J Orthop Translat 49 (2024) 167–180, https://doi.org/10.1016/j.jot.2024.08.004.
[4] H. Wang, J. Li, H. Feng, H. Hao, J. Ren, Y. Li, C. Li, J. Chen, C. Sun, J. Liang, G. Ning, S. Feng, Engineering injectable composite scaffolds for enhanced bone healing: Integration of stem cells, hydrogels, and microspheres, Chem. Eng. J. 507 (2025) 160593, https://doi.org/10.1016/j.cej.2025.160593.
[5] S. Dalfino, P. Savadori, M. Piazzoni, S.T. Connelly, A.B. Giannì, M. Del Fabbro, G. M. Tartaglia, L. Moroni, Regeneration of critical-sized mandibular defects using 3D-printed composite scaffolds: a quantitative evaluation of new bone formation in in vivo studies, Adv. Healthc. Mater. 12 (21) (2023) e2300128, https://doi.org/10.1002/adhm.202300128.
[6] Z. Zhou, W. Feng, B.K. Moghadas, N. Baneshi, B. Noshadi, S. Baghaei, D. A. Dehkordi, Review of recent advances in bone scaffold fabrication methods for tissue engineering for treating bone diseases and sport injuries, Tissue Cell 88 (2024) 102390, https://doi.org/10.1016/j.tice.2024.102390.
[7] M.P. Ferraz, An overview on the big players in bone tissue engineering: biomaterials, scaffolds and cells, Int. J. Mol. Sci. 25 (7) (2024), https://doi.org/10.3390/ijms25073836.
[8] W. Lan, X. Huang, D. Huang, X. Wei, W. Chen, Progress in 3D printing for bone tissue engineering: a review, J. Mater. Sci. 57 (27) (2022) 12685–12709, https://doi.org/10.1007/s10853-022-07361-y.
[9] J.R. Dias, A. Sousa, A. Augusto, P.J. Bártolo, P.L. Granja, Electrospun polycaprolactone (PCL) degradation: an in vitro and in vivo study, Polymers (Basel) 14 (2022), https://doi.org/10.3390/polym14163397.
[10] F. Fendi, B. Abdullah, S. Suryani, A.N. Usman, D. Tahir, Development and application of hydroxyapatite-based scaffolds for bone tissue regeneration: a systematic literature review, Bone 183 (2024) 117075, https://doi.org/10.1016/j.bone.2024.117075.
[11] D.B. Burr, M.A. Gallant, Bone remodelling in osteoarthritis, Nat. Rev. Rheumatol. 8 (11) (2012) 665–673, https://doi.org/10.1038/nrrheum.2012.130.
[12] H.J. Jang, J.K. Yoon, The role of vasculature and angiogenic strategies in bone regeneration, Biomimetics (Basel) 9 (2) (2024), https://doi.org/10.3390/biomimetics9020075.
[13] L. Zhang, X. Li, C. Shi, G. Ran, Y. Peng, S. Zeng, Y. He, Biocompatibility and angiogenic effect of chitosan/graphene oxide hydrogel scaffolds on EPCs, Stem Cells Int. 2021 (2021) 5594370, https://doi.org/10.1155/2021/5594370.
[14] Z. Chen, M. Jia, Y. Liu, H. Zhou, X. Wang, M. Wu, Injectable composite hydrogel stents for bone defect management with enhanced osteogenesis and angiogenesis, Int. J. Nanomedicine 20 (2025) 4589–4606, https://doi.org/10.2147/ijn.S509686.
[15] J. Lu, Y. Gao, C. Cao, H. Wang, Y. Ruan, K. Qin, H. Liu, Y. Wang, P. Yang, Y. Liu, Y. Ma, Z. Yu, Y. Wang, Z. Zhong, F. Chang, 3D bioprinted scaffolds for osteochondral regeneration: advancements and applications, Mater. Today Bio 32 (2025) 101834, https://doi.org/10.1016/j.mtbio.2025.101834.
[16] J.J. Li, C.R. Dunstan, A. Entezari, Q. Li, R. Steck, S. Saifzadeh, A. Sadeghpour, J. R. Field, A. Akey, M. Vielreicher, O. Friedrich, S.I. Roohani-Esfahani, H. Zreiqat, A novel bone substitute with high bioactivity, strength, and porosity for repairing large and load-bearing bone defects, Adv. Healthc. Mater. 8 (13) (2019) e1900641, https://doi.org/10.1002/adhm.201900641.
[17] P. Cai, C. Li, Y. Ding, H. Lu, X. Yu, J. Cui, F. Yu, H. Wang, J. Wu, M. El-Newehy, M. M. Abdulhameed, L. Song, X. Mo, B. Sun, Elastic 3D-printed nanofibers composite scaffold for bone tissue engineering, ACS Appl. Mater. Interfaces 15 (47) (2023) 54280–54293, https://doi.org/10.1021/acsami.3c12426.
[18] Y. Ding, M. Huang, P. Cai, X. Yu, J. Cui, B. Sun, X. Mo, C. Lu, J. Chen, J. Wu, Inflammation-modulating elastic decellularized extracellular matrix scaffold promotes meniscus regeneration, Acta Biomater. 196 (2025) 93–108, https://doi.org/10.1016/j.actbio.2025.02.043.
[19] K. Loukelis, V. Tsampallas, M. Kaliva, M. Vamvakaki, M. Chatzinikolaidou, Synthesis of N, N,O and O-carboxymethyl chitosan derivatives of controllable substitution degrees and their utilization as electrospun scaffolds for bone tissue engineering, Carbohydr. Polym. 348 (Pt A) (2025) 122775, https://doi.org/10.1016/j.carbpol.2024.122775.
[20] P. Cai, L. Cao, Y. Ding, Y. Han, X. Yu, J. Cui, H. Wang, J. Wu, M. El-Newehy, M. M. Abdulhameed, X. Mo, S. Wang, B. Sun, Modified highly elastic 3D nanofiber embolic scaffolds for precise in situ embolization therapy, Adv. Funct. Mater. 34 (27) (2024) 2316590, https://doi.org/10.1002/adfm.202316590.
[21] H. Lei, C. Song, Z. Liu, Z. Deng, J. Yu, F. Yuan, Y. Yang, Rational design and additive manufacturing of alumina-based lattice structures for bone implant, Mater. Des. 221 (2022) 111003, https://doi.org/10.1016/j.matdes.2022.111003.
[22] X. Zhou, J. Chen, H. Sun, F. Wang, Y. Wang, Z. Zhang, W. Teng, Y. Ye, D. Huang, W. Zhang, X. Mo, A. Liu, P. Lin, Y. Wu, H. Tao, X. Yu, Z. Ye, Spatiotemporal regulation of angiogenesis/osteogenesis emulating natural bone healing cascade for vascularized bone formation, J. Nanobiotechnol. 19 (1) (2021) 420, https://doi.org/10.1186/s12951-021-01173-z.
[23] A. Pal, RNA Sequencing (RNA-seq), Protocols in Advanced Genomics and Allied Techniques, Springer, US, New York, NY, 2022, pp. 279–322, https://doi.org/10.1007/978-1-0716-1818-9_13.
[24] R. Sedghi, A. Shaabani, N. Sayyari, Electrospun triazole-based chitosan nanofibers as a novel scaffolds for bone tissue repair and regeneration, Carbohydr. Polym. 230 (2020) 115707, https://doi.org/10.1016/j.carbpol.2019.115707.
[25] M. Weber, H. Steinle, S. Golombek, L. Hann, C. Schlensak, H.P. Wendel, M. Avci-Adali, Blood-contacting biomaterials: In vitro evaluation of the hemocompatibility,

Front. Bioeng. Biotechnol. 6 (2018) 99, https://doi.org/10.3389/fbioe.2018.00099.
[26] P. Yılmaz, E. Öztürk Er, S. Bakırdere, K. Ülgen, B. Özbek, Application of supercritical gel drying method on fabrication of mechanically improved and biologically safe three-component scaffold composed of graphene oxide/chitosan/hydroxyapatite and characterization studies, J. Mater. Res. Technol. 8 (6) (2019) 5201–5216, https://doi.org/10.1016/j.jmrt.2019.08.043.
[27] H.W. Lee, J.H. Shin, M. Simons, Flow goes forward and cells step backward: endothelial migration, Exp. Mol. Med. 54 (6) (2022) 711–719, https://doi.org/10.1038/s12276-022-00785-1.
[28] G.L. Semenza, Clinical investigation of hypoxia-inducible factors: getting there, J. Clin. Invest. 134 (3) (2024), https://doi.org/10.1172/jci176253.
[29] Y. Hao, W. Zhao, L. Zhang, X. Zeng, Z. Sun, D. Zhang, P. Shen, Z. Li, Y. Han, P. Li, Q. Zhou, Bio-multifunctional alginate/chitosan/fucoidan sponges with enhanced angiogenesis and hair follicle regeneration for promoting full-thickness wound healing, Mater. Des. 193 (2020) 108863, https://doi.org/10.1016/j.matdes.2020.108863.
[30] S. Song, G. Zhang, X. Chen, J. Zheng, X. Liu, Y. Wang, Z. Chen, Y. Wang, Y. Song, Q. Zhou, HIF-1α increases the osteogenic capacity of ADSCs by coupling angiogenesis and osteogenesis via the HIF-1α/VEGF/AKT/mTOR signaling pathway, J. Nanobiotechnol. 21 (1) (2023) 257, https://doi.org/10.1186/s12951-023-02020-z.
[31] Y. He, M.M. Sun, G.G. Zhang, J. Yang, K.S. Chen, W.W. Xu, B. Li, Targeting PI3K/Akt signal transduction for cancer therapy, Signal Transduct. Target. Ther. 6 (1) (2021) 425, https://doi.org/10.1038/s41392-021-00828-5.
[32] X.B. Cui, S.Y. Chen, Response gene to complement 32 in vascular diseases, Front. Cardiovasc. Med. 5 (2018) 128, https://doi.org/10.3389/fcvm.2018.00128.
[33] F.A. Abouelnazar, X. Zhang, J. Zhang, M. Wang, D. Yu, X. Zang, J. Zhang, Y. Li, J. Xu, Q. Yang, Y. Zhou, H. Tang, Y. Wang, J. Gu, X. Zhang, SALL4 promotes angiogenesis in gastric cancer by regulating VEGF expression and targeting SALL4/VEGF pathway inhibits cancer progression, Cancer Cell Int. 23 (1) (2023) 149, https://doi.org/10.1186/s12935-023-02985-9.
[34] Y. Kudo, S. Iizuka, M. Yoshida, T. Tsunematsu, T. Kondo, A. Subarnbhesaj, E. M. Deraz, S.B. Siriwardena, H. Tahara, N. Ishimaru, I. Ogawa, T. Takata, Matrix metalloproteinase-13 (MMP-13) directly and indirectly promotes tumor angiogenesis, J. Biol. Chem. 287 (46) (2012) 38716–38728, https://doi.org/10.1074/jbc.M112.373159.
[35] C. Lee, M.J. Kim, A. Kumar, H.W. Lee, Y. Yang, Y. Kim, Vascular endothelial growth factor signaling in health and disease: from molecular mechanisms to therapeutic perspectives, Signal Transduct. Target. Ther. 10 (1) (2025) 170, https://doi.org/10.1038/s41392-025-02249-0.
[36] H. Liu, M. Sun, N. Wu, B. Liu, Q. Liu, X. Fan, TGF-β/Smads signaling pathway, Hippo-YAP/TAZ signaling pathway, and VEGF: their mechanisms and roles in vascular remodeling related diseases, Immun. Inflamm. Dis. 11 (11) (2023) e1060.
[37] S. Monaci, F. Coppola, I. Filippi, A. Falsini, F. Carraro, A. Naldini, Targeting hypoxia signaling pathways in angiogenesis, Front. Physiol. 15 (2024) 1408750, https://doi.org/10.3389/fphys.2024.1408750.
[38] A. Ridiandries, J.T. Tan, C.A. Bursill, The role of CC-chemokines in the regulation of angiogenesis, Int. J. Mol. Sci. 17 (11) (2016), https://doi.org/10.3390/ijms17111856.
[39] M. Basheeruddin, S. Qausain, Hypoxia-inducible factor 1-alpha (HIF-1α): an essential regulator in cellular metabolic control, Cureus 16 (7) (2024) e63852, https://doi.org/10.7759/cureus.63852.
[40] K. Sonoda, S. Bogahawaththa, A. Katayama, S. Ujike, S. Kuroki, N. Kitagawa, K. Hirotsuru, N. Suzuki, T. Miyata, S.-I. Kawaguchi, T. Tsujita, Prolyl hydroxylase domain protein inhibitor not harboring a 2-oxoglutarate scaffold protects against hypoxic stress, ACS Pharmacol. Transl. Sci. 5 (5) (2022) 362–372, https://doi.org/10.1021/acsptsci.2c00002.
[41] X. Ma, S. Liu, B. Fan, D. Jin, L. Miao, L. Liu, S. Du, J. Lin, Enhancing mRNA translation efficiency by introducing sequence optimized AU-rich elements in 3′ UTR via HuR anchorage, Mol. Ther. Nucleic Acids 36 (2) (2025) 102485, https://doi.org/10.1016/j.omtn.2025.102485.
[42] J. Wlodarczyk, A. Leng, S.N. Abadchi, N. Shababi, F. Mokhtari-Esbuie, S. Gheshlaghi, M.R. Ravari, E.K. Pippenger, A. Afrasiabi, J. Ha, J.M. Abraham, J. W. Harmon, Transfection of hypoxia-inducible factor-1α mRNA upregulates the expression of genes encoding angiogenic growth factors, Sci. Rep. 14 (1) (2024) 6738, https://doi.org/10.1038/s41598-024-54941-w.
[43] Y. Liu, Z. Lin, J. Guo, G. Xu, Y. Li, T. Xu, H. Lv, J. Chen, G. Wu, Notoginsenoside R1 significantly promotes in vitro osteoblastogenesis, Int. J. Mol. Med. 38 (2) (2016) 537–544, https://doi.org/10.3892/ijmm.2016.2652.
[44] D. He, J. Ma, Z. Zhou, Y. Qi, Y. Lian, F. Wang, H. Yin, H. Zhang, T. Zhang, H. Huang, TET2 suppresses vascular calcification by forming an inhibitory complex with HDAC1/2 and SNIP1 independent of demethylation, J. Clin. Invest. 135 (9) (2025), https://doi.org/10.1172/jci186673.
[45] M.E. Schroeder, A. Gonzalez Rodriguez, K.F. Speckl, C.J. Walker, F.S. Midekssa, J. C. Grim, R.M. Weiss, K.S. Anseth, Collagen networks within 3D PEG hydrogels support valvular interstitial cell matrix mineralization, Acta Biomater. 119 (2021) 197–210, https://doi.org/10.1016/j.actbio.2020.11.012.